UNIVERSITY OF LEEDS

This is a repository copy of *Fibril structures of diabetes-related amylin variants reveal a basis for surface-templated assembly*.

White Rose Research Online URL for this paper:
https://eprints.whiterose.ac.uk/166728/

Version: Accepted Version

Article:
Gallardo, R orcid.org/0000-0003-1584-3564, Iadanza, MG, Xu, Y et al. (4 more authors) (2020) Fibril structures of diabetes-related amylin variants reveal a basis for surface-templated assembly. Nature Structural & Molecular Biology, 27 (11). pp. 1048-1056. ISSN 1545-9993

https://doi.org/10.1038/s41594-020-0496-3

© The Author(s), under exclusive licence to Springer Nature America, Inc. 2020. This is an author produced version of a paper published in Nature Structural & Molecular Biology. Uploaded in accordance with the publisher's self-archiving policy.

Reuse
Items deposited in White Rose Research Online are protected by copyright, with all rights reserved unless indicated otherwise. They may be downloaded and/or printed for private study, or other acts as permitted by national copyright laws. The publisher or other rights holders may allow further reproduction and re-use of the full text version. This is indicated by the licence information on the White Rose Research Online record for the item.

Takedown
If you consider content in White Rose Research Online to be in breach of UK law, please notify us by emailing eprints@whiterose.ac.uk including the URL of the record and the reason for the withdrawal request.

White Rose university consortium
Universities of Leeds, Sheffield & York

eprints@whiterose.ac.uk
https://eprints.whiterose.ac.uk/

Fibril structures of diabetes-related amylin variants reveal a basis for surface-templated assembly

Rodrigo Gallardo[1], Matthew G. Iadanza[1], Yong Xu[1], George R. Heath[2], Richard Foster[3], Sheena E. Radford[1‡] & Neil A. Ranson[1‡]

Astbury Centre for Structural Molecular Biology,

[1] School of Molecular & Cellular Biology

[2] School of Physics & Astronomy,

[3] School of Chemistry,
University of Leeds,
LS2 9JT, UK

‡ Corresponding authors: s.e.radford@leeds.ac.uk; n.a.ranson@leeds.ac.uk

Abstract

The aggregation of the peptide hormone amylin into amyloid deposits is a pathological hallmark of type-2 diabetes (T2D). While no causal link between T2D and amyloid has been established, the S20G mutation in amylin is associated with early-onset T2D. Here we report cryo-EM structures of amyloid fibrils of wild-type human amylin and its S20G variant. The wild-type fibril structure, solved to 3.6-Å resolution, contains two protofilaments, each built from S-shaped subunits. S20G fibrils, by contrast, contain two major polymorphs. Their structures, solved at 3.9-Å and 4.0-Å resolution, share a common two-protofilament core that is distinct from the wild-type structure. Remarkably, one polymorph contains a third subunit with another, distinct, cross-β conformation. The presence of two different backbone conformations within the same fibril may explain the increased aggregation propensity of S20G, and illustrates a potential structural basis for surface-templated fibril assembly.

Introduction

A cross-β structure was identified as the generic building block of amyloid fibrils over 50 years ago (reviewed in [1]). Famously associated with pathology in Alzheimer"s, Parkinson"s and Huntington"s diseases, amyloid fibrils formed by 36 human proteins have been associated with more than 50 diseases[1]. This stable amyloid fold also plays a functional role in bacteria, fungi, plants and man[2]. Driven by developments in cryo-electron microscopy (cryo-EM), electron diffraction and solid-state NMR, our understanding of amyloid structures has been revolutionized in recent years, with near-atomic resolution structures of amyloid fibrils formed *in vitro* and extracted from tissues of patients with Alzheimer"s disease[3,4], Picks disease[5], Chronic Traumatic Encephalopathy[6], Corticobasal degeneration[7], Multiple System Atrophy[8], and with systemic amyloidosis diseases caused by the misfolding of serum amyloid A[9], immunoglobulin light chains[10,11] and transthyretin[12]. These structures reveal a remarkable diversity of the common cross-β structure, with the same (or similar) protein sequences forming an array of structures, very different to the one sequence–one structure relationship common to globular proteins. This body of work has also shown that different fibril structures formed by the same, or similar, protein sequence can result in different diseases, as illustrated by fibrils from disease-associated variants of α-synuclein in Parkinson"s disease (PD) and dementia with Lewy bodies (DLB)[13,14], or the 8 different fibril structures currently determined for different isotypes of tau associated with Alzheimer"s disease, Pick"s disease, Chronic Traumatic Encephalopathy and Corticobasal Degeneration[3,5-7].

The aggregation of the 37-residue peptide hormone amylin (human islet amyloid polypeptide) into amyloid fibrils has been linked to type-2 diabetes (T2D)[15], in which amyloid deposition in pancreatic islets is a recognized histopathological hallmark. Amylin is co-secreted with insulin by pancreatic β-cells and is essential for glucose homeostasis. While no direct causal link between amylin and T2D has been established, numerous reports implicate amylin and its amyloid formation in β-cell death[16,17]. Importantly, a single genetic mutation in amylin causing the S20G variant is associated with a familial, early onset form of T2D[18]; this substitution renders amylin more aggregation-prone and increases risk of disease[19-21].

Biochemical experiments have shown that peptides spanning the amylin sequence from residues 8 to 37 can form amyloid aggregates[22], with the sequence $_{22}$NFGAIL$_{27}$ playing a central role in amyloid formation[23-25]. By X-ray crystallography, it has been shown that several fragments of amylin can assemble into amyloid-like assemblies with different backbone conformations[26,27]. While it is improbable that all of these very different homotypic interactions could occur simultaneously in amyloid fibrils formed from full-length amylin, these structures show that a single amylin fragment can adopt different conformations to stabilize an amyloid fold, consistent with polymorphism seen in other protein fibrils[3,5-7,9,11].

Here, we describe a 3.6-Å-resolution structure of amylin amyloid fibrils formed *in vitro* from the wild-type protein, as well as fibrils with two different structures formed by the S20G variant, at 3.9 Å and 4.0 Å resolution. The results show that wild-type amylin fibrils are formed from two protofilaments each containing a single amylin subunit per molecular layer. The subunits adopt an S-shaped conformation in each protofilament, reminiscent the structures of fibrils formed by the Alzheimer‟s disease-associated Aβ_{42} peptide[28-31], which has a similar length and has 56% sequence similarity in its central aggregation prone region. The structures of the S20G variant show that the serine to glycine substitution results in a different protofilament fold at the core of the fibril. Strikingly, this new fold generates a surface onto which a third subunit, with a completely different backbone conformation, binds. This arrangement generates a unique three-protofilament fibril that contains three asymmetric amylin subunits per molecular layer. This lateral association may represent the molecular basis of surface-catalysed amyloid growth via secondary nucleation, and a potential mechanism for increased aggregation of the S20G variant.

Results

Polymorphism in amylin amyloid fibrils

We synthesized peptides corresponding to wild-type human amylin and the S20G variant, using solid phase peptide synthesis. Peptides were C-terminally amidated and contained the native disulfide bridge between residues 2 and 7. Purity and completeness of disulfide formation were assessed by HPLC and electrospray ionisation mass spectrometry (ESI-MS), respectively (Supplementary Fig. 1). Both wild-type amylin and the S20G variant formed amyloid fibrils within 2 days of incubation under identical conditions at pH 6.8 (Methods), as judged by negative stain EM (Extended Data Fig. 1). Both samples are polymorphic. For wild-type amylin the predominant polymorph, that accounts for ~80% of all fibrils imaged using cryo-EM, is long (>1 μm) and thin (<20 nm in diameter), and has an overt crossover length of ~25 nm (Fig. 1a and Extended Data Fig. 1a, b). Fibrils of the S20G variant were more heterogeneous, but the majority (~79% of all fibrils imaged) present an overt crossover length of ~50 nm (Fig. 1b and Extended Data Fig. 1c,d). We did not identify any fibrils with a

25 nm crossover (i.e. the „wild-type morphology") in the S20G fibril samples, but fibrils with a 50 nm crossover (i.e. the „S20G morphology") were found in the wild-type sample (~10%), as judged by atomic force microscopy (AFM), although these were almost never observed in cryo-EM. All fibrils of all polymorphs, both wild-type and S20G, have an unambiguous left-handed helical twist as judged by AFM (Fig. 1a, b insets; Extended Data Fig. 1e, f). The fibril height profiles, obtained using AFM, confirms the predominant crossover lengths observed by EM, at 22 ± 2 nm for wild-type and 43 ± 5 nm for S20G fibrils.

Cryo-EM structure of wild-type amylin fibrils

The wild-type fibril sample described above was used for cryo-EM analyses (Methods). After manual selection from the raw micrographs and 2D and 3D classification, we obtained a homogeneous dataset of segments from the fibrils with a 25 nm crossover length (Extended Data Fig. 2a-e), from which a 3D structure was determined at 3.6-Å resolution (Table 1). The reconstruction has two symmetric protofilaments consisting of stacked layers of density (Fig. 2). Each subunit is characterized by a continuous density that corresponds to the peptide backbone, preceded at one end by a Localized Disordered Region (LDR)[32] (Fig. 2a), and has a helical twist of 178.23º and rise of 2.43 Å, characteristic of a left-handed, 2_1-screw axis symmetry. This led to a left-handed helical fibril in which the layers of density in each protofilament are separated by β-strand spacing of ~4.9 Å (Fig. 2b, c and Sup. Fig. 2a). However, the layers are not perpendicular to the fibril long axis, but are tilted by ~10º in opposite directions in each protofilament (Fig. 2d and Extended Data Fig. 3a-c). This tilt means that each monomer "i" contacts four different monomers in the opposing protofilaments ("j-1", "j", "j+1" and "j+2") at its C-terminal (residue Y37) and central regions (residues 21–27). Each layer in each protofilament can accommodate a single amylin subunit (Fig. 2e). The quality of the density was sufficient to build an unambiguous model for the C-terminal 23 residues of the wild-type amylin sequence (residues 14–37), consistent with a wealth of biochemical, biophysical and structural information that this region is most likely to be structured in the fibril core[22,23,33-36]. The density of the bulky side chains of F15, H18, F23 and Y37 are consistent with this interpretation (Fig. 2e). Each monomer folds into a planar, S-shaped backbone conformation forming three β-strands (β1: residues 14–19, β2: 26–31 and β3: 35-36) separated by two loops (L1: residues 20–25 and L2: 32–34) (Fig. 2e; Extended Data Fig. 3d).

The loop L1 contains a substantial portion of the inter-protofilament interface where residues $_{23}$FGA$_{25}$ pack against the same region in the opposite protofilament forming a homotypic, face-to-face, dry-steric zipper stabilized by two main chain-main chain interactions consistent with H-bonds between the zipper residues (Fig. 2e, panel i). The tilt of each monomer is especially important in this region as the main-chain H-bonds of a monomer "i" in one protofilament bond to different opposing monomers in its same plane ("j") and above its plane ("j+1") in the opposite protofilament (Extended Data Fig. 3a-c). This arrangement generates a network of interactions consistent with H-bonds that expands across the inter-protofilament interface (Fig. 2e, panel i). The rest of the inter-protofilament interface is generated by the formation of a hydrophobic core consisting of residue F23 with A25, L27 and Y37 of the opposing monomer (Fig. 2e, panel ii).

Intra-monomer interactions that stabilize the S-shaped fold involve both hydrophobic (V17 and I26 (Fig. 2e)) and polar interactions (S29, N31, N35, Y37 (Fig. 2e, panel iii)). There are also extensive inter-layer interactions consistent with H-bonds via the formation of asparagine ladders (N21 (Fig. 2e, panel iv), N22 and N35). Collectively, these interactions define two cores in each protofilament. A first core forms a tube of polar residues along the fibril and is predominantly formed by residues S29, N31, N35, together with T30 and the phenolic -OH of Y37. The second core is apolar and is formed by residues F15, V17, I26, together with the residues at the inter-protofilament interface (Fig. 2e). In combination, these fibrils employ all of the stabilizing features observed in amyloid fibrils formed from other proteins and peptides to date, contained within a single structure: homotypic dry zippers, polar and apolar cores, aromatic stacking, asparagine ladders and the formation of parallel β-sheets.

S20G fibrils contain two distinct polymorphs

A cryo-EM dataset of S20G fibrils was also collected. Fibrils were manually selected from the raw cryo-EM images, and after 2D classification an apparently homogeneous dataset of fibril segments consistent with a ~50 nm crossover length was obtained, and in which β-strands appear to be out of register as judged from the 2D-class averages (Extended Data Fig. 4a-g; Supplementary Figure 2b-c).

Extensive subsequent 3D classifications suggested that the dataset contains two similar structures with an identical overt crossover length. Once this had been established, we were able to solve one of these structures to 3.9 Å and discovered that it contained three protofilaments. We then used this structure as model for further rounds of 3D classification to separate the dataset into its component parts. These separated datasets were then each solvable, generating two fibrils, one with two protofilaments (2PF; 4.0-Å resolution; ~76% of the fibril segments with a 50 nm repeat) and one with three protofilaments (3PF; 3.9-Å resolution; ~24% of the fibril segments with a 50 nm repeat), which we describe below.

Cryo-EM structure of the 2PF fibril

The 2PF fibril contains two identical monomers per molecular layer, one in each protofilament (Fig. 3a, b). Each of these monomers adopts a planar (Fig 3c, d), two-dimensional structure that is tilted away from the plane perpendicular to the fibril long axis by approximate 1.7º (Extended Data Fig. 5). The layers in each protofilament are out of register with each other by precisely half of the inter-strand spacing (2.4-Å) (Fig. 3d), which corresponds to a 2_1 pseudo-screw symmetry with a twist of 179.05º per subunit (Table 1). Each monomer contains four β-strands formed by residues 15–18 (β1), 21–23 (β2), 28–31(β3) and 35–36 (β4) (Fig. 3e and Extended Data Fig. 3d). Strands β1, β3 and β4 partially overlap in sequence with strands β1, β2 and β3 observed in the wild-type structure, respectively while strand β2 from S20G is not observed in the wild-type structure (Extended Data Fig. 3d).

The spatial arrangement of secondary structure elements in the S20G 2PF structure is completely different to that in the wild-type fibrils. In fact, the backbone of these structures cannot be superposed (Extended Data Fig. 6a); only the segment containing residues $_{31}$NVGSNT$_{36}$ can be superposed between these structures (RMSD 0.95 Å; Extended Data

Fig. 6b). The interface between the protofilaments is also less interdigitated in the S20G 2PF structure, and is formed by residues $_{25}$AIL$_{27}$ that arrange in a face-to-face, homotypic, dry steric zipper (Fig. 3e, panel i). These amino acids are consecutive to those that form the interface in the wild-type structure ($_{23}$FGA$_{25}$), but neither the interfacial nor the adjacent residues can be superposed between wild-type and 2PF structures. Both polar and apolar interactions stabilize the 2PF monomer fold. The apolar interactions are between residues F23, I26 and V32 (Fig. 3e, panel ii), whilst the polar interactions involve side chain-side chain contacts between residues H18 and N21, and between N31 and N35 (Fig. 3e, panel iii). Some of the interactions that stabilize the stacking of monomers are conserved between wild-type and S20G structures, these include common features of amyloid fibrils such as the stacking of the aromatic side chains of residues F15, F23 and Y37.

The structure of the S20G fibrils shows a single apolar core within each S20G monomer formed by residues F23, I26 and V32 and the $_{25}$AIL$_{27}$ sequence at the interface between protofilaments (Fig. 3e). This core extends across the interface between monomers and constitutes a large hydrophobic region that gives stability to the protofilaments that form the 2PF fibril, and is shielded from the solvent by patches of polar residues form by residues S19 to N22 and S28 to N31 on the surface of the fibril (Fig. 3e). There is also a polar core that contributes to the stability of the fibril formed by side chains of H18 from β1, N21 from β2 and S34 and β4 (Fig. 3e, panel iii).

The 3PF and 2PF fibrils share a common core architecture.

The second major polymorph found in the S20G sample is an unprecedented structure that we term 3PF, and is composed of three monomers per molecular layer each of which stack to generate three protofilaments (Fig. 4). One of these monomers (protofilament C, shown in red in Fig. 4b–f) has a completely different fold to the other two monomers (protofilaments A and B; blue and green respectively in Fig. 4b, c) the latter of which are symmetrical, and have a backbone conformation that is indistinguishable (at 3.9-Å resolution) from the two monomers in a layer of the 2PF structure. Indeed, the backbone superposition of the symmetrical monomers A and B observed in 3PF fibrils with those of 2PF fibrils has a RMSD of ~1.7 Å over 23 residues (Extended Data Fig. 6c). Moreover, the symmetric monomers in 3PF are also out of register (Fig. 4c, d) and related by a 2_1 pseudo-screw axis symmetry as observed in the 2PF fibrils, with a very similar interface (residues $_{25}$AIL$_{27}$) engaged in a homotypic, apolar steric zipper (Fig. 4e, f). Despite their similarities, the relative tilt angles and stacking arrangement of subunits in protofilaments A and B in 3PF fibrils are subtly different to those observed in 2PF fibrils, presumably because of the binding of the third monomer on one side of the “2PF-like” core, which inserts its C-terminal end into the groove between protofilaments A and B (Fig. 4e, f) and distorts the even spacing between monomeric planes observed in the 2PF fibrils (Extended Data Fig. 5e-g). Instead, this generates an alternating short distance (~1.33 Å) and long distance (~3.44 Å) between monomeric planes (Extended Data Fig. 5h).

The outcome of the docking of protofilament C onto the fibril side is that the molecular layers of 3PF are rendered asymmetric by the presence of the monomers in protofilament C. This asymmetry and the distortion of the spacing between monomer planes means that the 3PF polymorph cannot be reconstructed by applying the same symmetry operators of 2PF. Instead this polymorph was reconstructed by applying C1 symmetry with a helical rise of 4.81 Å and twist per subunit of 358.1º (Table 1).

The subunits within the symmetric, "2PF-like" core of the 3PF fibril have the same β-strands and interconnecting loops observed in the S20G 2PF fibril (Extended Data Fig. 3d). In contrast, the monomers in protofilament C have only two β-strands (β1: residues 15-18 and β2: residues 25-29) which partially overlap with β1 and β2 observed the wild-type structure (Extended Data Fig. 3d). Indeed, subunits in protofilament C are more similar to those in the wild-type structure than those in protofilaments A & B to which they are opposed. The superposition of the backbone of monomer C (red in Fig. 4b, c, e) and the wild-type monomer has an RMSD of 3.1 Å over the 14 N-terminal residues observed in the structure (residues 15-29), indicating that they have, in part, a similar fold (Extended Data Fig. 6d). Unlike protofilaments A and B in the 3PF structure, the monomers in protofilament C are neither planar nor perpendicular to the fibril axis. The insertion of the C-terminus of monomer C into the groove between protofilaments A and B is above the plane of the neighbour monomer B. The rest of the chain of monomer C descends along the fibril axis and enters in register with the monomer B by its N-terminal region (Fig. 4d and Extended Data Fig. 5e). Through the insertion of their C-terminal ends, monomers in protofilament C interact with monomers in both protofilaments A and B. The side chain of the C-terminal Y37 in monomer C contacts the side-chains of L27 and S28 in an A-type monomer, while its backbone makes an interaction consistent with an H-bond with the side-chain of N22 in a B-type monomer B (Fig. 4f). The interface between monomer B and monomer C is larger than that between monomers A and B, and it is formed by both polar and apolar residues that cluster at two different points of the interface (Fig. 4e). The apolar interactions are between residues A25, L27 of the asymmetric monomer C with F15 and V17 on the neighbour monomer B. The polar interactions are between S29 of monomer C and S19 of monomer B. The polar cluster also includes the side chains N31 and T36 of monomer C, and N22 of monomer B. The backbone of monomer C describes a broad turn in this position, which is 12 Å away from the backbone of monomer B at its most distant point. As consequence there is a loose interdigitation of the residues in the polar patch (Fig. 4e). The 3PF fibrils therefore strongly resemble a 2PF fibril with the addition of a third monomer with a unique fold, and constitute an unprecedented three protofilament asymmetric amyloid fibril structure.

Symmetric and asymmetric interfaces in the wild-type, 2PF and 3PF fibrils

The structures described highlight how the single substitution S20G results in large differences in the conformation of amylin subunits that form the protofilaments of the amyloid fibrils (Fig. 5a, b & c) and in profoundly different protofilament interfaces (Fig. 5d, e & f), even though the sidechain of residue 20 does not participate in fibril-stabilizing interfaces and is solvent-exposed in both wild-type and S20G polymorphs (Fig. 5d, e & f). To understand how the difference in protofilament interfaces might influence fibril stability, we analyzed the different interfaces using the software PDBePISA[37]. We generated fibril segments of six molecular layers organized in two protofilaments for wild-type and S20G 2PF fibrils (Figs. 2 & 3) or three protofilaments for 3PF fibrils (Fig. 4) and compared their buried surface area, solvation free energy gain upon formation of the interface ($\Delta^{i}G$), and the free energy of assembly dissociation (ΔG^{diss}) (Table 2).

In the wild-type fibril, the buried surface area between protofilaments is 1960 Å^2. The $\Delta^{i}G$ for the interface is ~ -28 kcal/mol, and the ΔG^{diss} of the fibril into two protofilaments is ~ 22 kcal/mol. If the number of molecular layers is then decreased and the ΔG^{diss} re-evaluated, a

minimum length for the fibril to be considered stable can be obtained ($\Delta G^{diss} > 0$) which, for the wild-type structure, is two layers (giving a ΔG^{diss} of ~0.4 kcal/mol) (Extended Data Fig. 6e). In the S20G 2PF fibril, the inter-protofilament interface is 360 Å^2, confirming the visual impression of a smaller interface. The $\Delta^i G$ of the interface between protofilaments is ~ -9 kcal/mol, and the ΔG^{diss} of the two protofilaments is only ~ -2 kcal/mol, which suggests that the minimum length for a stable S20G 2PF fibril would be 7 or more molecular layers. Finally, the combined interface areas between the monomers in each molecular layer of the 3PF fibril was determined to be 2571 Å^2, the combined $\Delta^i G$ of these interfaces is ~ -42 kcal/mol, and the ΔG^{diss} is ~9 kcal/mol. Decreasing the number of molecular layers for this polymorph suggests that the minimum length for a 3PF fibril to be stable would be four molecular layers, in which case ΔG^{diss} is ~3 kcal/mol. Hence, as expected by their larger buried surface area, the 3PF fibrils are predicted to be significantly more stable than their 2PF counterpart.

The interface between all protofilaments in 3PF fibrils can be broken down into two sub-interfaces (Table 2). The interface between symmetric monomers (A and B in Fig. 4) is similar to that in the S20G 2PF fibril (Fig. 3), but the presence of the asymmetric monomer expands the hydrophobic core of the fibril (Fig. 5f) and distorts the spacing between planes of symmetric monomers (Extended Data Fig. 5h). We estimate that the total buried area of this "2PF-like" interface is ~482 Å^2. This is greater than that of the S20G 2PF, and results in a $\Delta^i G$ of ~ -12 kcal/mol and ΔG^{diss} of ~1 kcal/mol. The interface between monomer B and monomer C in 3PF fibrils is larger than that between monomers A and B. The estimated buried area in this interface is ~1644 Å^2, its $\Delta^i G$ is ~ -20 kcal/mol and its ΔG^{diss} is ~ 5 kcal/mol. Therefore, the predicted dissociation pattern for 3PF fibrils would be for the interface between symmetric monomers (i.e. A & B) to break first, with that between asymmetric partners (i.e. B & C) being more resilient.

Discussion

Here we present the structures of amyloid fibrils of wild-type amylin at 3.6 Å resolution and two major polymorphs of the S20G variant associated with early-onset T2D (at 4.0 and 3.9 Å resolution) [18,38]. Two recent papers have reported cryo-EM structures of wild-type amylin fibrils. Röder et al.[39] describe three polymorphs, the most abundant of which had its structure determined at 4.2-Å-resolution; this polymorph had a 25 nm crossover length and a monomer fold that is very similar to the wild-type structure described here (within the resolution limit of the reconstructions; Extended Data Fig. 7a). However, based on AFM analysis of dried fibrils, the structure by Röder *et al*. is a right-handed fibril, whereas AFM of hydrated material created here shows that the fibrils are unambiguously left-handed, consistent with previous reports for wild-type amylin fibrils with a 25 nm repeat[23,40,41]. Cao et al[42] report a completely different architecture for fibrils formed by an N-terminally SUMOylated amylin variant, again with two protofilaments. However, that monomer fold is unrelated to the one reported here (Extended Data Fig. 7b), perhaps due to the addition of a SUMO tag (~13 kDa) that is substantially larger than amylin itself (~4 kDa).

The wild-type amylin fibril structure obtained here is different from that determined previously using solid-state NMR[43], which was derived from a sample containing two major polymorphs. One polymorph (described as a "striated ribbon") also contained two symmetric amylin molecules per layer, but each formed two parallel β-sheets connected by a loop

(Extended Data Fig. 8a, b); the other polymorph (described as a “twisted fibril”) with a period of 25 to 50 nm and height of 4 to 10 nm, was not structurally elucidated, but it may correspond to the wild-type amylin fibrils here (25 nm repeat, height 8 nm). Importantly, the experimental conditions in our study are different from those employed by others who also observed twisted amylin fibrils[23,35,40], suggesting that this twisted morphology is an inherent feature of amylin amyloids.

The wild-type amylin structure presented here is consistent with previous biochemical[22,23], bioinformatic[35] and structural studies[33,34,36] that collectively suggest that the N-terminal region does not form part of the fibril core, that the C-terminal region is folded, and that Y37 is buried in a quasi-crystalline state[44]. The overall S-shape of the monomers within the wild-type amylin protofilaments is reminiscent of a previous “β-serpentine” model for amylin amyloid (Extended Data Fig. 8c, d)[35]. Previous X-ray crystal structures of short segments of amylin covered most of the residues visible in our structure and showed that several of those segments self-interact, and do so in multiple conformations[26,27,45,46]. Six of those fragment structures superpose on the cryo-EM structure of wild-type amylin presented here[27,46] (Extended Data Fig. 8e), including one that covers the inter-protofilament interface[27] ($_{21}$NNFGAIL$_{27}$). This fragment structure overlays almost perfectly with our structure (RMSD ~0.4 Å, Extended Data Fig. 8f), but the interface itself cannot be reproduced based on the fragment structure as it does not capture the tilted relationship between monomers in the fibril.

Many of the features previously observed to contribute to the stability of other amyloid fibrils are also present in the wild-type amylin fibril structure. These include asparagine ladders[30], where residue N21 (Fig. 2d, panel iv) is particularly interesting as the substitution N21P increases the rate of amylin aggregation, possibly by inducing a turn in the backbone[47], consistent with its position in our structure. Other stabilizing features include interactions between each monomer and multiple monomers in the opposing protofilament. Such interactions have been observed in fibrils of Aβ$_{42}$ prepared *in-vitro*[29] and in *ex-vivo* fibrils extracted from systemic AA amyloidosis patients[9]. This feature is particularly important in the wild-type amylin fibril (Extended Data Fig. 3a-c) but also in the interaction of monomer C with the core of 3PF fibrils (Extended Data Fig. 5e, g). Finally, both wild-type and S20G amylin fibrils are stabilized by (different) polar and apolar interactions (Fig. 5d, e & f). In particular, H18 was reported to play a role in Zn^{2+} binding[48], and it is surface-exposed in wild-type fibrils, but buried in 2PF and 3PF, suggesting these fibrils could have different zinc-binding properties (Extended Data Fig. 9a,b). Inter-protofilament interfaces of pathological amyloids seem to contain mostly apolar cores, as observed in fibrils of human prion protein[49], Aβ$_{40/42}$ [29,30,50], and α-synuclein[51]. By contrast, the structure of Orb2, a functional amyloid implicated in memory persistence in Drosophila[52], featured exclusively polar interfaces. Here the interface between monomers B and C in S20G 3PF fibrils contains both apolar and polar cores (Fig. 5f). Whether this particular interface composition gives 3PF fibrils distinctive properties regarding its thermodynamic stability, or characteristic kinetics of assembly or disassembly, remain to be studied.

The S-shaped monomer in wild-type amylin fibrils is reminiscent of structures of the Alzheimer‟s disease-related Aβ$_{42}$ fibrils determined using ssNMR[28,30,31] and cryo-EM[29]. The clinical relationship between Alzheimer's and T2D has been known for some time[53], and the risk of dementia (including Alzheimer‟s disease and vascular dementia, both linked to Aβ deposition) is increased in patients with T2D[54]. Indeed, a recent study linked T2D to a subset

of dementias termed Diabetes-related Dementia (DrD)[55]. The molecular explanation for this link remains unclear, but it may involve cross-seeding of aggregation[56] possibly via direct interaction of aggregation-prone regions[57]. A superposition of the wild-type amylin fibrils here with those of $A\beta_{42}$ (Extended Data Fig. 10a-e) supports this hypothesis, as noted previously[39]. Indeed, the most similar segments in amylin and $A\beta_{42}$ (residues 10–27 in amylin, 15–32 in $A\beta_{42}$, Extended Data Fig. 10a) include the inter-protofilament interfaces in both wild-type and S20G amyloid structures. Whether co-aggregation results from cross-seeding, co-aggregation, secondary nucleation or association between preformed protofilaments remains unresolved[58,59]. Strikingly, superposition of the amylin and $A\beta_{42}$ fibril structures shows that the disease-related mutations (S20G in amylin and E22G in $A\beta_{42}$ (also known as the Arctic mutation) occupy structurally equivalent positions[39] (Extended Data Fig. 10b). However, it is not possible to predict whether the effects of the Arctic mutation in Alzheimer"s disease[60] arise from structural manifestations in the architecture of $A\beta_{42}$ fibrils akin to those described here for amylin.

The effects of the S20G substitution in amylin on fibril architecture are unanticipated and remarkable. The wild-type and 2PF structures have distinct folds, inter-protofilament interfaces, steric zippers and stabilizing cores, but S20 is solvent exposed in each. The 3PF structure is unprecedented, revealing a single fibril composed of two different protofilament structures: a "2PF-like" core with the lateral association of a third protofilament. There are currently four structures of amyloid fibrils with three protofilaments: unseeded *in vitro* fibrils of $A\beta_{40}$[61] and of the D23N "Iowa" mutant of $A\beta_{40}$[50], *in vitro* seeded fibrils from an Alzheimer"s disease brain sample[62] and the *ex* vivo extracted functional Orb2 amyloid fibrils from Drosophila brains[52]; in each case the fibrils are symmetric. By contrast, the backbone fold of subunit C of the S20G 3PF fibrils is completely different to that of the subunits A and B in the same fibril. Thus, the same amylin sequence is able to adopt multiple conformations, even within the same molecular assembly, a phenomenon strikingly reminiscent of how quasi-equivalence is utilized by viruses to build their capsids[63].

Although the precision of the stabilities of the different fibrils and their interfaces is limited by the resolution of the structural data presented here, PDBePISA establishes a clear trend: wild-type fibrils are most stable, followed by the S20G 3PF fibril, with the S20G 2PF fibril being the least thermodynamically favourable structure. However, 2PF fibrils are more common than 3PF fibrils. This is consistent with the aggregation of S20G being under kinetic control, wherein aggregation into the 3PF polymorph is thermodynamically favourable, but occurs from a nucleation event that is rarer. The observation that S20G aggregates more rapidly than wild-type amylin is consistent with such a hypothesis[19-21]. An alternate explanation is that 3PF arises directly from a 2PF core, via seeding of a new protofilament on the preformed fibril surface. If this were the case, the 3PF structure shown here would describe the structural details of the kind of interactions that support secondary nucleation. Detailed study of the aggregation kinetics of S20G, together with analysis of large cryo-EM datasets acquired at different time-points within the aggregation reaction, will likely shed light on this in the future.

Acknowledgements

R.G., Y.X., R.F., N.A.R. & S.E.R thank Wellcome for generous support (204963). M.G.I is supported by the MRC (MR/P018491/1). All EM was performed at the Astbury Biostructure

Laboratory which was funded by the University of Leeds and the Wellcome Trust (108466/Z/15/Z), and we thank Rebecca Thompson, Emma Hesketh, Dan Maskell & Charlotte Scarff for assistance with cryo-EM data collection. We thank Valentina Zorzini for assistance in model building. Peptide synthesis was performed using instrumentation funded by EPSRC (EP/N013573/1). The AFM experiments were performed with instrumentation funded by Wellcome (101497/Z/13/Z). All data processing was performed using ARC4 at the University of Leeds. Finally, we thank colleagues in the Radford and Ranson laboratories for many helpful discussions while preparing this manuscript.

Author contributions

R.G., M.G.I., Y.X., R.F., S.E.R. & N.A.R. designed the experiments. Y.X. synthesized and characterized peptides, R.G. and Y.X. optimized fibril growth conditions and prepared fibrils. R.G. and G.R.H. performed the AFM experiments. R.G. prepared EM samples and collected data. R.G. and M.G.I. performed image processing and reconstruction. R.G. performed model building and refinement. All authors analysed some or all of the data, and wrote or edited the manuscript.

Competing interests

The authors have no competing interests

References

1. Iadanza, M.G., Jackson, M.P., Hewitt, E.W., Ranson, N.A. & Radford, S.E. A new era for understanding amyloid structures and disease. *Nat Rev Mol Cell Biol* **19**, 755-773 (2018).
2. Otzen, D. & Riek, R. Functional Amyloids. *Cold Spring Harb Perspect Biol* **11**, DOI: 10.1101/cshperspect.a033860 (2019).
3. Fitzpatrick, A.W.P. et al. Cryo-EM structures of tau filaments from Alzheimer's disease. *Nature* **547**, 185-190 (2017).
4. Kollmer, M. et al. Cryo-EM structure and polymorphism of Abeta amyloid fibrils purified from Alzheimer's brain tissue. *Nat Commun* **10**, 4760 (2019).
5. Falcon, B. et al. Structures of filaments from Pick's disease reveal a novel tau protein fold. *Nature* **561**, 137-140 (2018).
6. Falcon, B. et al. Novel tau filament fold in chronic traumatic encephalopathy encloses hydrophobic molecules. *Nature* **568**, 420-423 (2019).
7. Zhang, W. et al. Novel tau filament fold in corticobasal degeneration. *Nature* **580**, 283-287 (2020).
8. Schweighauser, M. et al. Structures of alpha-synuclein filaments from multiple system atrophy. *Nature*, DOI: 10.1038/s41586-020-2317-6 (2020).
9. Liberta, F. et al. Cryo-EM fibril structures from systemic AA amyloidosis reveal the species complementarity of pathological amyloids. *Nat Commun* **10**, 1104 (2019).
10. Radamaker, L. et al. Cryo-EM structure of a light chain-derived amyloid fibril from a patient with systemic AL amyloidosis. *Nat Commun* **10**, 1103 (2019).
11. Swuec, P. et al. Cryo-EM structure of cardiac amyloid fibrils from an immunoglobulin light chain AL amyloidosis patient. *Nat Commun* **10**, 1269 (2019).

12. Schmidt, M. et al. Cryo-EM structure of a transthyretin-derived amyloid fibril from a patient with hereditary ATTR amyloidosis. *Nat Commun* **10**, 5008 (2019).
13. Boyer, D.R. et al. Structures of fibrils formed by alpha-synuclein hereditary disease mutant H50Q reveal new polymorphs. *Nat Struct Mol Biol* **26**, 1044-1052 (2019).
14. Boyer, D.R. et al. The alpha-synuclein hereditary mutation E46K unlocks a more stable, pathogenic fibril structure. *Proc Natl Acad Sci U S A* **117**, 3592-3602 (2020).
15. Westermark, P., Wernstedt, C., Wilander, E. & Sletten, K. A novel peptide in the calcitonin gene related peptide family as an amyloid fibril protein in the endocrine pancreas. *Biochem Biophys Res Commun* **140**, 827-31 (1986).
16. Birol, M., Kumar, S., Rhoades, E. & Miranker, A.D. Conformational switching within dynamic oligomers underpins toxic gain-of-function by diabetes-associated amyloid. *Nat Commun* **9**, 1312 (2018).
17. Raleigh, D., Zhang, X., Hastoy, B. & Clark, A. The beta-cell assassin: IAPP cytotoxicity. *J Mol Endocrinol* **59**, R121-R140 (2017).
18. Sakagashira, S. et al. Missense mutation of amylin gene (S20G) in Japanese NIDDM patients. *Diabetes* **45**, 1279-81 (1996).
19. Meier, D.T. et al. The S20G substitution in hIAPP is more amyloidogenic and cytotoxic than wild-type hIAPP in mouse islets. *Diabetologia* **59**, 2166-71 (2016).
20. Sakagashira, S. et al. S20G Mutant Amylin Exhibits Increased in Vitro Amyloidogenicity and Increased Intracellular Cytotoxicity Compared to Wild-Type Amylin. *Am. J. Pathol.* **157**, 2101-2109 (2000).
21. Young, L.M., Tu, L.H., Raleigh, D.P., Ashcroft, A.E. & Radford, S.E. Understanding co-polymerization in amyloid formation by direct observation of mixed oligomers. *Chem Sci* **8**, 5030-5040 (2017).
22. Jaikaran, E.T. et al. Identification of a novel human islet amyloid polypeptide beta-sheet domain and factors influencing fibrillogenesis. *J Mol Biol* **308**, 515-25 (2001).
23. Goldsbury, C. et al. Amyloid fibril formation from full-length and fragments of amylin. *J Struct Biol* **130**, 352-62 (2000).
24. Westermark, P., Engstrom, U., Johnson, K.H., Westermark, G.T. & Betsholtz, C. Islet amyloid polypeptide: pinpointing amino acid residues linked to amyloid fibril formation. *Proc Natl Acad Sci U S A* **87**, 5036-40 (1990).
25. Ashburn, T.T.a.A., Michele and Lansbury, Peter T. The structural basis of pancreatic amyloid formation: isotope-edited spectroscopy in the solid state. *J. Am. Chem. Soc.* **114**, 790-791 (1992).
26. Soriaga, A.B., Sangwan, S., Macdonald, R., Sawaya, M.R. & Eisenberg, D. Crystal Structures of IAPP Amyloidogenic Segments Reveal a Novel Packing Motif of Out-of-Register Beta Sheets. *J. Phys. Chem. B* **120**, 5810-6 (2016).
27. Wiltzius, J.J. et al. Atomic structure of the cross-beta spine of islet amyloid polypeptide (amylin). *Protein Sci* **17**, 1467-74 (2008).
28. Colvin, M.T. et al. Atomic Resolution Structure of Monomorphic Abeta42 Amyloid Fibrils. *J. Am. Chem. Soc.* **138**, 9663-74 (2016).
29. Gremer, L. et al. Fibril structure of amyloid-beta(1-42) by cryo-electron microscopy. *Science* **358**, 116-119 (2017).
30. Walti, M.A. et al. Atomic-resolution structure of a disease-relevant Abeta(1-42) amyloid fibril. *Proc Natl Acad Sci U S A* **113**, E4976-84 (2016).
31. Xiao, Y. et al. Abeta(1-42) fibril structure illuminates self-recognition and replication of amyloid in Alzheimer's disease. *Nat Struct Mol Biol* **22**, 499-505 (2015).

32. Gallardo, R., Ranson, N.A. & Radford, S.E. Amyloid structures: much more than just a cross-beta fold. *Curr Opin Struct Biol* **60**, 7-16 (2020).
33. Alexandrescu, A.T. Amide proton solvent protection in amylin fibrils probed by quenched hydrogen exchange NMR. *PLoS One* **8**, e56467 (2013).
34. Jayasinghe, S.A. & Langen, R. Identifying structural features of fibrillar islet amyloid polypeptide using site-directed spin labeling. *JBC* **279**, 48420-48425 (2004).
35. Kajava, A.V., Aebi, U. & Steven, A.C. The parallel superpleated beta-structure as a model for amyloid fibrils of human amylin. *J. Mol. Biol.* **348**, 247-252 (2005).
36. Weirich, F. et al. Structural Characterization of Fibrils from Recombinant Human Islet Amyloid Polypeptide by Solid-State NMR: The Central FGAILS Segment Is Part of the beta-Sheet Core. *PLoS ONE* **11**, e0161243 (2016).
37. Krissinel, E. & Henrick, K. Inference of macromolecular assemblies from crystalline state. *J Mol Biol* **372**, 774-97 (2007).
38. Seino, S. & Study Group of Comprehensive Analysis of Genetic Factors in Diabetes, M. S20G mutation of the amylin gene is associated with Type II diabetes in Japanese. Study Group of Comprehensive Analysis of Genetic Factors in Diabetes Mellitus. *Diabetologia* **44**, 906-9 (2001).
39. Röder, C. et al. Cryo-EM structure of islet amyloid polypeptide fibrils reveals similarities with amyloid-beta fibrils. *Nat Struct Mol Biol* **27**, 660-667 (2020).
40. Goldsbury, C.S. et al. Polymorphic fibrillar assembly of human amylin. *J Struct Biol* **119**, 17-27 (1997).
41. Bedrood, S. et al. Fibril structure of human islet amyloid polypeptide. *J Biol Chem* **287**, 5235-41 (2012).
42. Cao, Q., Boyer, D.R., Sawaya, M.R., Ge, P. & Eisenberg, D.S. Cryo-EM structure and inhibitor design of human IAPP (amylin) fibrils. *Nat Struct Mol Biol* **27**, 653-659 (2020).
43. Luca, S., Yau, W.M., Leapman, R. & Tycko, R. Peptide conformation and supramolecular organization in amylin fibrils: constraints from solid-state NMR. *Biochemistry* **46**, 13505-22 (2007).
44. Padrick, S.B. & Miranker, A.D. Islet amyloid polypeptide: identification of long-range contacts and local order on the fibrillogenesis pathway. *J Mol Biol* **308**, 783-94 (2001).
45. Krotee, P. et al. Common fibrillar spines of amyloid-beta and human islet amyloid polypeptide revealed by microelectron diffraction and structure-based inhibitors. *J Biol Chem* **293**, 2888-2902 (2018).
46. Wiltzius, J.J. et al. Molecular mechanisms for protein-encoded inheritance. *Nat Struct Mol Biol* **16**, 973-8 (2009).
47. Godin, E., Nguyen, P.T., Zottig, X. & Bourgault, S. Identification of a hinge residue controlling islet amyloid polypeptide self-assembly and cytotoxicity. *J Biol Chem* **294**, 8452-8463 (2019).
48. Rowinska-Zyrek, M. Coordination of Zn(2+) and Cu(2+) to the membrane disrupting fragment of amylin. *Dalton Trans* **45**, 8099-106 (2016).
49. Glynn, C. et al. Cryo-EM structure of a human prion fibril with a hydrophobic, protease-resistant core. *Nat Struct Mol Biol* **27**, 417-423 (2020).
50. Sgourakis, N.G., Yau, W.M. & Qiang, W. Modeling an in-register, parallel "iowa" aβ fibril structure using solid-state NMR data from labeled samples with rosetta. *Structure* **23**, 216-227 (2015).

51. Li, B. et al. Cryo-EM of full-length alpha-synuclein reveals fibril polymorphs with a common structural kernel. *Nat Commun* **9**, 3609 (2018).
52. Hervas, R. et al. Cryo-EM structure of a neuronal functional amyloid implicated in memory persistence in Drosophila. *Science* **367**, 1230-1234 (2020).
53. Han, W. & Li, C. Linking type 2 diabetes and Alzheimer's disease. *Proc Natl Acad Sci U S A* **107**, 6557-8 (2010).
54. Biessels, G.J., Staekenborg, S., Brunner, E., Brayne, C. & Scheltens, P. Risk of dementia in diabetes mellitus: a systematic review. *Lancet Neurol* **5**, 64-74 (2006).
55. Hanyu, H. Diabetes-Related Dementia. *Adv Exp Med Biol* **1128**, 147-160 (2019).
56. Hu, R., Zhang, M., Chen, H., Jiang, B. & Zheng, J. Cross-Seeding Interaction between beta-Amyloid and Human Islet Amyloid Polypeptide. *ACS Chem. Neurosci.* **6**, 1759-68 (2015).
57. Andreetto, E. et al. Identification of hot regions of the Abeta-IAPP interaction interface as high-affinity binding sites in both cross- and self-association. *Angew Chem Int Ed Engl* **49**, 3081-5 (2010).
58. O'Nuallain, B., Williams, A.D., Westermark, P. & Wetzel, R. Seeding specificity in amyloid growth induced by heterologous fibrils. *J Biol Chem* **279**, 17490-9 (2004).
59. Young, L.M. et al. Insights into the consequences of co-polymerisation in the early stages of IAPP and Abeta peptide assembly from mass spectrometry. *Analyst* **140**, 6990-9 (2015).
60. Nilsberth, C. et al. The 'Arctic' APP mutation (E693G) causes Alzheimer's disease by enhanced Abeta protofibril formation. *Nat Neurosci* **4**, 887-93 (2001).
61. Paravastu, A.K., Leapman, R.D., Yau, W.M. & Tycko, R. Molecular structural basis for polymorphism in Alzheimer's beta-amyloid fibrils. *Proc Natl Acad Sci U S A* **105**, 18349-54 (2008).
62. Lu, J.X. et al. Molecular structure of beta-amyloid fibrils in Alzheimer's disease brain tissue. *Cell* **154**, 1257-68 (2013).
63. Caspar, D.L. & Klug, A. Physical principles in the construction of regular viruses. *Cold Spring Harb Symp Quant Biol* **27**, 1-24 (1962).

Figure legends

Figure 1. Morphology of amylin fibrils. Raw cryoEM images of (a) wild-type amylin, and (b) S20G amylin fibrils. Overt cross-over lengths of 25 nm (wild-type) and 50 nm (S20G) are indicated by white arrows. All fibrils have a left-handed twist, as indicated by AFM (inset to a & b).

Figure 2. Structure of the protofilaments and near atomic resolution model for the wild-type amylin fibril. (a) Cross-sections through unsharpened 3D reconstructions for wild-type and its schematic representation showing an ordered core composed of two protofilaments surrounded by diffuse density for more poorly-resolved regions of the map. (b) Cross section with the two protofilaments of wild-type fibrils coloured blue (protofilament A) and green (protofilament B). (c) 45º tilt of (b). (d) Two molecular layers, the upper one coloured as in (b) and (c), and the lower one, in identical view, with the density coloured according to height (in) along the fibril long axis, as indicated in the key (with zero corresponding to the centre of mass of the molecular layer). (e) The two, symmetry-related

subunits each comprise a protofilament (A in blue, and B in green). (e(i)) Main chain H-bonds across the inter-protofilament interface between F23 of one subunit and A25 of the other, zig-zag up and down the interface; (ii) a hydrophobic core stabilizes the inter-protofilament interface and the subunit fold; (iii) polar residues stabilize the subunit fold; and (iv) stacking of aromatic sidechains and asparagine ladders stabilize the fibril.

Figure 3. Conformation of the S20G 2PF fibrils and details of its molecular structure. (a) Cross-sections through unsharpened 3D reconstructions for S20G 2PF fibrils and its schematic representation showing two protofilaments in an ordered core surrounded by diffuse density for more poorly-resolved regions of the map. (b) Fibril cross section in an identical view and colouring as that shown in Figure 2b. (c) Side view of the out of register stacking of layers in the two protofilaments. (d) The two protofilaments coloured by height along the fibril axis. (e) The atomic model with and without the density from which it is derived. (d(i)) Shows the interface between protofilaments, dominated by interactions between A25 in one protofilament and L27 in the other; (ii) depicts the hydrophobic core of the subunit fold; and (iii) polar interactions stabilizing the subunit fold, especially involving H18 that is solvent exposed in the wild-type structure.

Figure 4. Conformation of the S20G 3PF fibrils and details of its molecular structure. (a) Cross-sections through unsharpened 3D reconstructions for S20G 3PF fibrils and its schematic representation showing three protofilaments in an ordered core surrounded by diffuse density for more poorly resolved regions of the map. (b) Cross section view with the two protofilaments that resemble the 2PF fibrils coloured blue (protofilament A) and green (protofilament B), and an additional protofilament associated on one face of the fibril, coloured in red (protofilament C). (c) Side view. (d) Single layer coloured by height along the fibril axis. (e) Atomic model with the density from which it is derived. (f) The C-terminus of protofilament C, interdigitates into the gap between protofilaments A and B.

Figure 5. Schematic views of the backbone fold and inter-protofilament interactions in the structures of wild-type, S20G 2PF and S20G 3PF amylin fibrils. (a, b and c) show the amylin backbone represented as a tube, and coloured as a rainbow from the N -terminal (N; blue) to C-terminal (C; red) residues observed in the structure (residues 14-37) for (a) wild-type, (b) S20G 2PF and (c) S20G 3PF fibrils. (d, e and f) shows the backbone trace of each monomer for (d) wild-type, (e) S20G 2PF and (f) S20G 2PF fibrils. The backbones are coloured by protofilament, as in Figures 2-4, and the amino acid side-chains are schematically represented by spheres. The sequence number for selected amino acids is indicated by numbers coloured according to the protofilament they refer to. The one-letter code is used to identify each amino acid. Polar and apolar cores that extend across protofilament interfaces are indicated by green and yellow regions, respectively.

Table 1. Cryo-EM data collection, refinement and validation statistics.

	Wildtype (EMD-11380, PDB 6ZRF)	S20G - 2PF (EMD-11382, PDB Z6RQ)	S20G – 3PF (EMD-11383, PDB 6ZRR)
Data collection and processing			
Magnification	130,000	130,000	
Voltage (kV)	300	300	
Electron exposure (e^{-}/Å^2)	1.01	1.05	
Defocus range (μm)	-1.3 to -2.9, step 0.2	-0.6 to -2.8, step 0.2	
Pixel size (Å)	1.065	1.065	
Symmetry imposed	*C1*	*C1*	
Initial particle images (no.)	117,316	64,274	
Final particle images (no.)	32,846	11,901	6,447
Helical Twist	178.23º	179.05º	358.1º
Helical rise (Å)	2.43	2.41	4.81
Map resolution (Å)	3.6	4.0	3.9
FSC threshold	0.143	0.143	0.143
Refinement			
Initial model used	*de novo*	*de novo*	*de novo*
Model resolution (Å)	3.9	4.4	4.5
FSC threshold	0.5	0.5	0.5
Map sharpening *B* factor (Å^2)	-150	-93	-98
Model composition			
Non-hydrogen atoms	2200	2040	3060
Protein residues	288	276	396
R.M.S. deviations			
Bond lengths (Å)	0.010	0.006	0.010
Bond angles (°)	0.9	1.172	1.175
Validation			
MolProbity score	2.41	2.20	2.29
Clashscore	38	23.19	29.63
Favored rotamers (%)	95	94	96
Poor rotamers (%)	0	0	0
Ramachandran plot			
Favored (%)	95	95	95
Allowed (%)	5	5	5
Disallowed (%)	0	0	0

Table 2. Protofilament interface analysis of wildtype, S20G 2PF and S20G 3PF fibrils.

	Wildtype	S20G 2PF	S20G 3PF
$\Delta^{i}G$ (kcal/mol)	– 28.3	– 8.8	– 41.5 A–B interface: –12.1 B–C interface: –20.0
Surface area (Å^2)	10662	11068	14320
Protofilament interface area (Å^2)	1960	360	2571 A–B interface: 482 B–C interface: 1644
ΔG^{diss} (kcal/mol)	22	–1.7	8.6 A–B interface: 1.1 B–C interface: 5.2
No. and type of monomer based on structure	12 A	12 A	12 A + 6 B
Protofilament species	AB	AB	ABC
Dissociation	A+B	A+B	A+BC
Minimal fibril length (rungs)	2	≥7	4

Methods

Preparation of wild-type and S20G amylin peptide

Wild-type and S20G amylin were synthesized using a Liberty Blue™ automated microwave peptide synthesiser (CEM Microwave Technology) on a 0.1 mmol scale as reported previously[64,65]. 9-fluorenylmethyloxycarbonyl (Fmoc)-protected amino acids were used, and PAL-NovaSyn TG resin (Merck) was selected, allowing the generation of amylin with an amidated C-terminus. Three pseudoproline dipeptides (Fmoc-Ala-Thr(psiMe,MePro)-OH, Fmoc-Ser(tBu)-Ser(psiMe,MePro)-OH, and Fmoc-Leu-Ser(psiMe,Mepro)-OH, Merck) were used for the synthesis of Ala-8 and Thr-9, Ser-19 and Ser-20, and Leu-27 and Ser-28. All the residues and the three pseudoproline dipeptides were double coupled. The peptides were cleaved from the resin in a cleavage cocktail of trifluoroacetic acid (TFA) (9.4 mL), 3,6-dioxa-1,8-octanedithiol (DODT) (250 µL), H_2O (250 µL), and triisopropylsilane (TIS) (100 µL). The mixture was stirred at room temperature for 3.5 hours and then concentrated under a nitrogen stream. Subsequently, the crude peptide was precipitated in cold diethyl ether, followed by three washes with the same solvent. The peptide was then dissolved in a 50% acetonitrile aqueous solution containing 0.1% TFA, and lyophilized. The peptide was then dissolved in 50% DMSO aqueous solution to promote the formation of the internal disulfide bond between Cys-2 and Cys-7. The oxidized peptides were then purified by reverse-phase, high-performance liquid chromatography (HPLC) using a Kinetex™ EVO C18 column (Phenomenex). The buffers used in the HPLC purification were acetonitrile with 0.1% formic acid and H_2O with 0.1% formic acid. The masses of the purified peptides were confirmed by Electrospray Ionisation Mass Spectrometry (ESI-MS) as 3902.9 for wt amylin (expected=3903.3), and as 3872.9 for amylin-S20G (expected=3873.3). The purity of the two peptides was assessed by analytical HPLC and was >95%. After purification peptides were again lyophilized and stored at -20ºC until use.

Fibril Growth

Lyophilized peptides where monomerized by dissolution into hexafluoroisopropanol (Sigma) at a final concentration of 1 mg/ml. The sample were incubated by 15 minutes at room temperature with occasional agitation to allow complete monomerization. The monomerized samples where then aliquoted in 1.5 ml glass vials containing 50 µg of peptide per vial. The solvent was evaporated to dryness by gently blowing a stream of nitrogen gas while swirling around the vial so as to generate a film of peptide around the walls of the vial. The vials containing dried peptide films were stored at -20ºC until use. At the moment of use, peptide vials were allowed to reach room temperature before opening, and then an aliquot of ice-cold aggregation buffer (freshly prepared 20 mM ammonium acetate, pH 6.8 filtrated through 0.2 µm PDVF filter right before use) was added so as to obtain stock concentrations not higher than 100 µM of peptide. The concentration of the stock was estimated by Absorbance at 280 nm using the calculated molar extinction coefficient of 1615 $M^{-1}cm^{-1}$. The concentration of the stocks was adjusted to 30 µM by addition of aggregation buffer and the samples were incubated quiescently at room temperature to allow the formation of amyloid fibrils that was confirmed by negative stain TEM and ThT fluorescence. Typically, amyloid fibrils were observed within 24 to 48 hours. After the observation of fibrils, samples where kept at 4ºC until their use for cryo-EM sample preparation and where used within two weeks of its preparation.

AFM sample preparation and imaging

The handedness of fibrils was unambiguously determined using AFM. A sample volume of 40 µl of either wild-type (at 30 µM) or S20G amylin fibrils (at 15 µM), was deposited onto freshly cleaved mica and allowed to incubate for 4 min. The mica surface was then rinsed with buffer (50 mM Na-PO_4, 300mM KCl, pH 7.5) via fluid exchange, maintaining the fibrils in a liquid environment. AFM observations were performed in tapping mode using a Dimension FastScan Bio with FastScan-D-SS probes (Bruker) in the same buffer. The force applied by the tip on the sample was minimized by maximizing the set point whilst maintaining tracking of the surface.

Cryo-electron microscopy imaging

Amylin fibrils (either wild-type or S20G) at a concentration of 30 µM monomer equivalent were diluted 1:2 with fibril buffer supplemented with 300 mM NaCl to achieve a final concentration of 15 µM monomer equivalent of the peptides. A 300-mesh copper EM grid with lacey carbon film (Agar Scientific) was glow discharged in a Tergeo-EM plasma cleaner (Pie Scientific) for 1 min at 40 mA power. Four microlitres of the sample was applied to the grid, which was then blotted with Whatman #40 filter paper and plunge-frozen in liquid ethane using a Vitrobot mark IV (ThermoFisher).

EM images were collected using a Titan Krios (Thermo Fisher) electron microscope operating at 300 keV and recorded on an energy filtered K2 direct detector (Gatan) with a pixel size of 1.06 /pi xel. For wild-type sample a set of 800 micrographs were recorded with a defocus range between -1.3 and -2.9 µm every 0.2 µm, and total electron doses of 50.7 $e^-/Å^2$. The dose was fractionated into 50 frames for per frame doses of 1.01 $e^-/Å^2$. For S20G sample a set of 684 micrographs were recorded with a defocus range between -0.6 and -2.8

μm every 0.2 μm, and total electron doses of 54.7 $e^-/Å^2$. The dose was fractionated into 52 frames for per frame doses of 1.05 $e^-/Å^2$.

Frames 3 to 50 of wild-type micrograph movies, and 3 to 52 of S20G micrograph movies were motion-corrected, dose weighted, and merged using motioncor2[66]. The contrast transfer function (CTF) for each micrograph was determined using gCTF[67] on motion-corrected, but non-dose weighted, micrographs.

Helical reconstruction

Helical reconstruction[68] was performed using Relion3.0[69] except for initial model generation which was performed in Relion 3.1[70]. The data were assessed by eye and start and end points for fibrils that appeared to be composed of a single set of protofilaments were interactively selected by hand. For S20G data-set the fibrils were segmented into 300x300 pixel boxes (corresponding to 319.5 Å x 319.5 Å), with an overlap of 90% (an offset of 30 px, 31.95 Å). For wild-type data-set the fibrils were segmented into 200x200 pixel boxes (corresponding to 213.0 Å x 213.0 Å), with an overlap of 90% (an offset of 20 px, 21.3 Å). For the wild-type data-set the initial 117316 extracted segments were subjected to multiple rounds of 2D classification, at each iteration of refinement classes showing an obvious ~4.8 Å repeating feature were taken forward into the next classification iteration. The 84597 segments ultimately take forward from this iterative 2D classification process were then subjected to iterative rounds of 3D classification using a *de novo* starting model generated by Relion 3.1. The same procedure was followed for the S20G data-set, where 64274 segments where extracted initially, and after multiple rounds of 2D classification, where only those classes showing an obvious ~4.8 Å repeating feature were taken forward into the next classification iteration, yielded a final set of 25137 segments that were taken forward to iterative rounds of 3D classification using a *de novo* starting model generated by Relion 3.1[70].

The initial 3D classification rounds where performed with searching of helical rise and twist around values estimated from crossover lengths measured from 2D class averages. In these classification steps the wild-type and S20G data-sets were separated into 3 classes each. After the first round of classification the initial model was updated to that showing the best separation of density stacks along the fibril axis. For wild-type, after several rounds of update of initial model a final 3D classification was performed with fixed values of 178.23º helical twist and 2.43 Å helical rise.

For S20G the initial 3D classification with search of helical rise and twist yielded two distinct polymorphs, which contained either two or three protofilaments. We followed the 3D classification strategy employed for the wildtype data-set using the obtained three protofilaments model as initial model for the next 3D classification round. This allowed us to separate the particles contributing to the three protofilament structure, form those that contributed to the two protofilament structure. The class of particles belonging to the three protofilament structure was further 3D classified with searches of helical symmetry. The symmetry searches converged to values for rise and twist of 4.81 Å and 358.1°, respectively. The class showing the best separation of stacks of density along the helical axis was used as initial model for a new 3D classification round with fixed helical parameters found in the precedent step. The resulting model of was employed as initial model for a 3D classification against the original mixed data set into two-protofilament, three-protofilament, and

ambiguous classes. This step generated a class containing 6447 for the 3PF reconstruction. The particles contributing to the 2PF structure where 3D classified using the 2PF map as starting model. The symmetry searches converged to values for rise and twist of 2.41 Å and 179.05°, respectively. A final 3D classification with the resulting model and fixed helical parameters against the 2PF particles resulted in a class that containing 11901 particles.

Each of the resulting 3D classes were subjected to 3D refinement using their respective 3D maps as reference maps and a T value of 50 and fixed helical parameters. After refinement all models were masked (wild-type: 15% of Z length; S20G: 10% of Z length) and post-processed in Relion. Fourier shell correlation plots for wild-type, S20G 2PF and S20G 3PF are show in Supplementary Fig. 3.

Model building and refinement.

Atomic models of single layers for each of the fibril reconstruction maps were built *de novo* in Coot[71]. The initial model of S20G 2PF was used to guide the model building of 3PF. For each of the models 6 copies of the single layer models were fit into the respective cryo-EM maps using Chimera[72] to preserve nearest neighbour interactions during subsequent refinement steps. The stack of 6 layers was then subjected to multiple rounds of real-space refinement with in Phenix[73] alternated with real-space refinement in COOT. The refinements in Phenix were restrained by defining non-crystallographic symmetry restrain groups for each of the protofilaments. Side-chain clashes were detected using MOLPROBITY[74] and corrected by iterative cycles of real-space refinement in COOT and real-space refinement in Phenix. All refinements were performed using information to 3.6 Å resolution for wild-type, 3.9 Å resolution for S20G 2PF and 4.0 Å resolution for S20G 3PF.

Further information on experimental design is available in the Nature Research Reporting Summary linked to this article.

Data availability

The cryo-EM maps and atomic models have been deposited in the EMDB and wwPDB, respectively, with the following accession codes: wild-type amylin (EMD-11380, PDB 6ZRF), S20G 2PF (EMD-11382, PDB 6ZRQ), and S20G 3PF (EMD-11383, PDB 6ZRR).

Methods-only references

64. Abedini, A. & Raleigh, D.P. The role of His-18 in amyloid formation by human islet amyloid polypeptide. *Biochemistry* **44**, 16284-91 (2005).
65. Khemtemourian, L., Guillemain, G., Foufelle, F. & Killian, J.A. Residue specific effects of human islet polypeptide amyloid on self-assembly and on cell toxicity. *Biochimie* **142**, 22-30 (2017).
66. Zheng, S.Q. et al. MotionCor2: anisotropic correction of beam-induced motion for improved cryo-electron microscopy. *Nat Methods* **14**, 331-332 (2017).
67. Zhang, K. Gctf: Real-time CTF determination and correction. *J Struct Biol* **193**, 1-12 (2016).

68. He, S. & Scheres, S.H.W. Helical reconstruction in RELION. *J Struct Biol* **198**, 163-176 (2017).
69. Zivanov, J. et al. New tools for automated high-resolution cryo-EM structure determination in RELION-3. *Elife* **7**, e42166 (2018).
70. Scheres, S.H.W. Amyloid structure determination in RELION-3.1. *Acta Crystallogr D Struct Biol* **76**, 94-101 (2020).
71. Emsley, P., Lohkamp, B., Scott, W.G. & Cowtan, K. Features and development of Coot. *Acta Crystallogr D Biol Crystallogr* **66**, 486-501 (2010).
72. Pettersen, E.F. et al. UCSF Chimera--a visualization system for exploratory research and analysis. *J Comput Chem* **25**, 1605-12 (2004).
73. Liebschner, D. et al. Macromolecular structure determination using X-rays, neutrons and electrons: recent developments in Phenix. *Acta Crystallogr D Struct Biol* **75**, 861-877 (2019).
74. Chen, V.B. et al. MolProbity: all-atom structure validation for macromolecular crystallography. *Acta Crystallogr D Biol Crystallogr* **66**, 12-21 (2010).

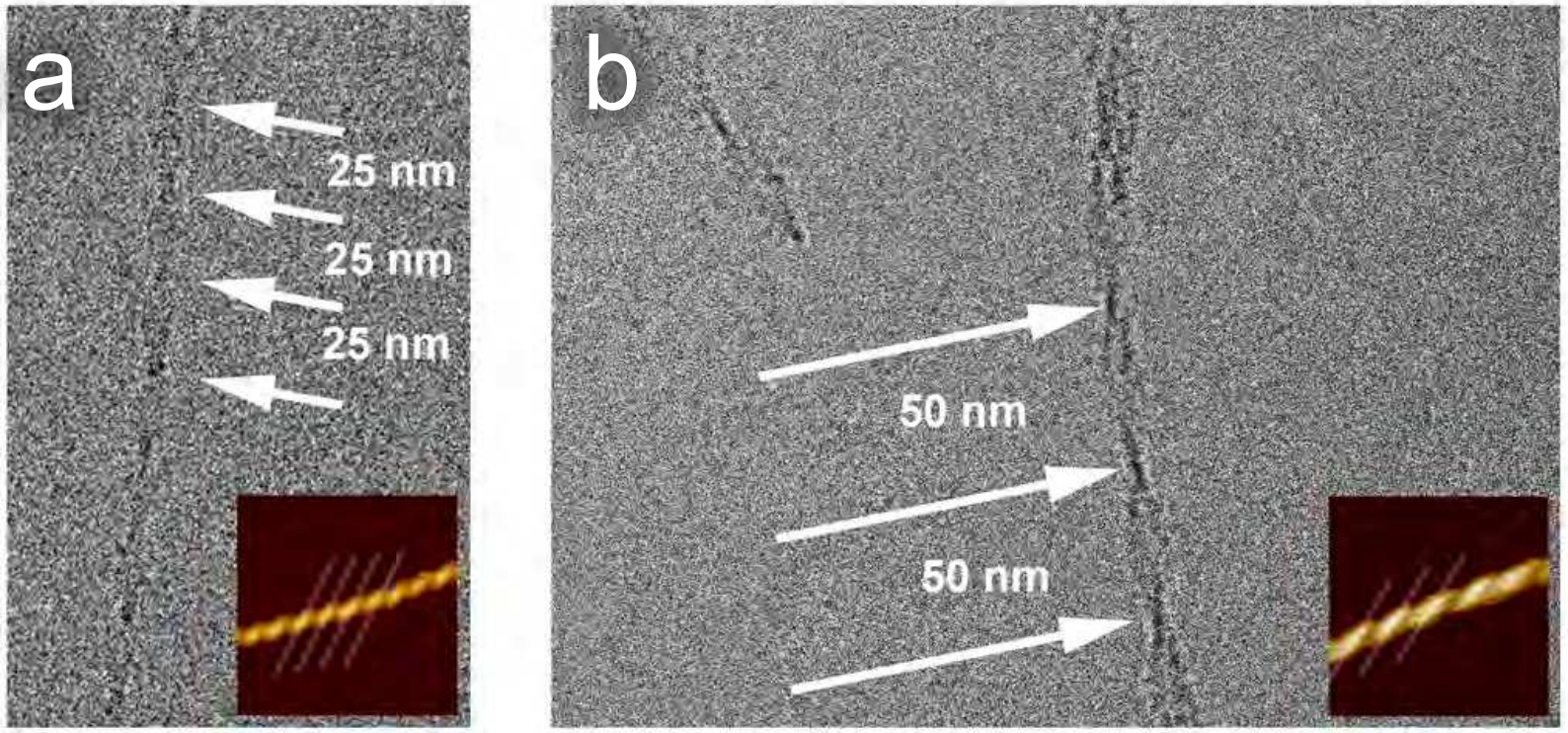
a
25 nm
25 nm
25 nm
b
50 nm
50 nm

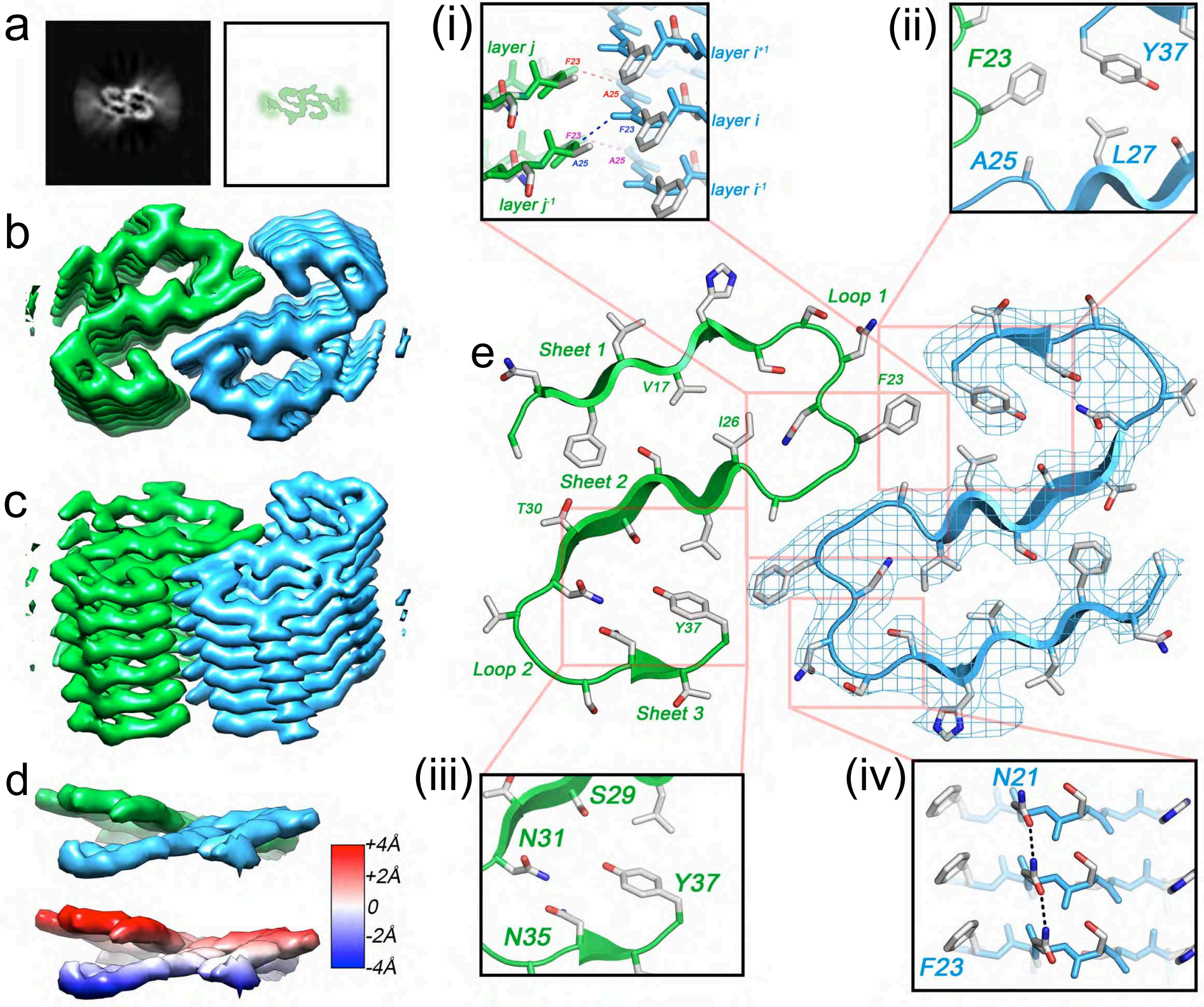
a
b
c
d
+4Å
+2Å
0
-2Å
-4Å
(i)
layer j
layer i+1
layer i
layer i-1
layer j-1
F23
A25
(ii)
F23
Y37
A25
L27
e
Loop 1
Sheet 1
V17
F23
I26
Sheet 2
T30
Y37
Loop 2
Sheet 3
(iii)
S29
N31
Y37
N35
(iv)
N21
F23

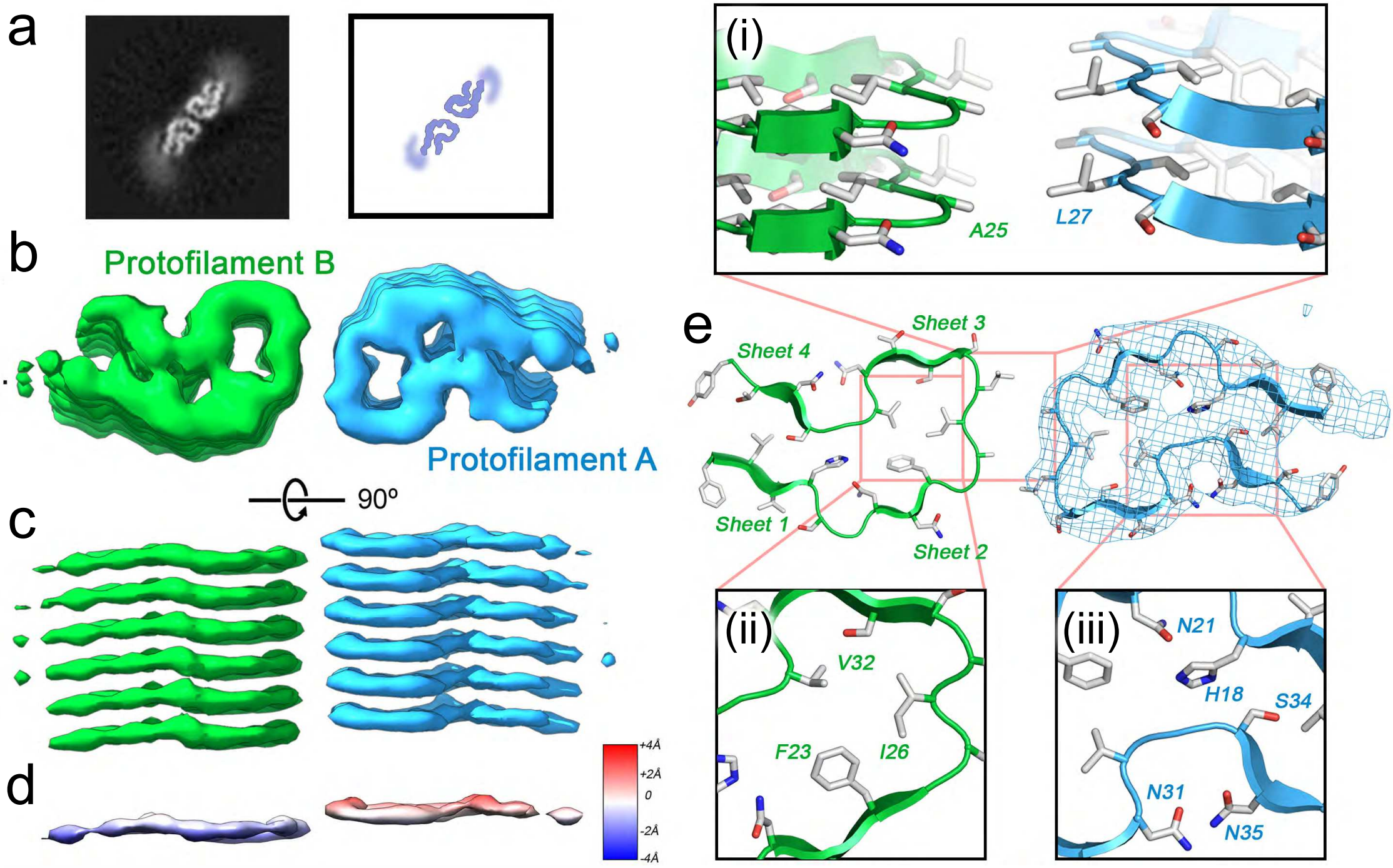
a
b
Protofilament B
Protofilament A
90°
c
d
+4Å
+2Å
0
-2Å
-4Å
e
Sheet 4
Sheet 3
Sheet 1
Sheet 2
(i)
A25
L27
(ii)
V32
F23
I26
(iii)
N21
H18
S34
N31
N35

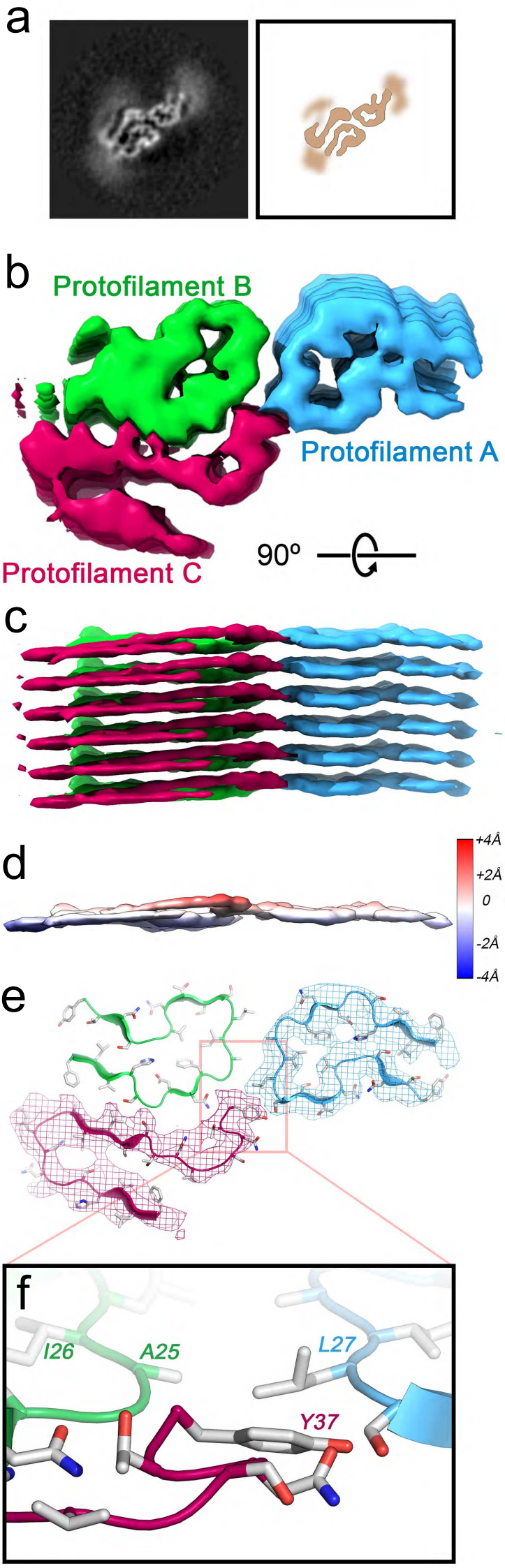
a
b
Protofilament B
Protofilament A
Protofilament C
90°
c
d
+4Å
+2Å
0
-2Å
-4Å
e
f
I26
A25
L27
Y37

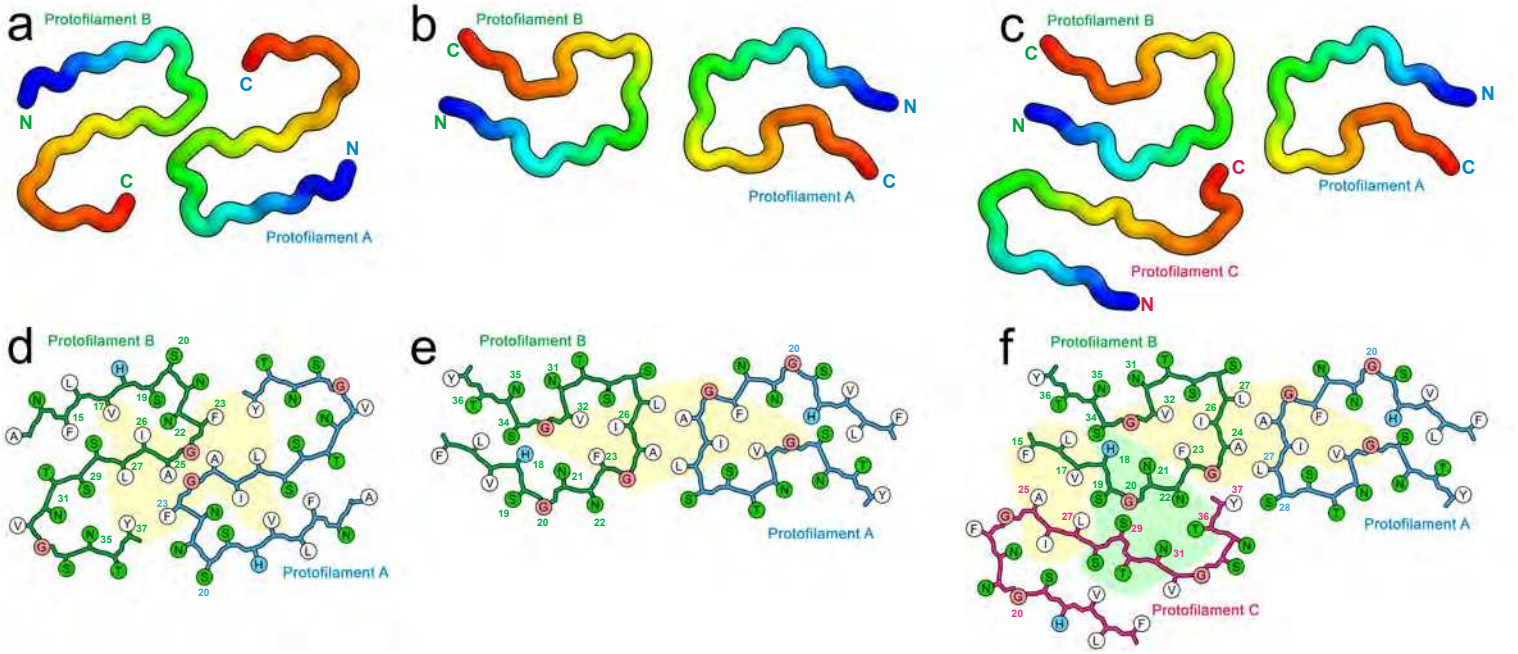
a
Protofilament B
N
C
C
N
Protofilament A
b
Protofilament B
C
N
N
C
Protofilament A
c
Protofilament B
C
N
C
N
Protofilament A
Protofilament C
N
d
Protofilament B
Protofilament A
e
Protofilament B
Protofilament A
f
Protofilament B
Protofilament A
Protofilament C

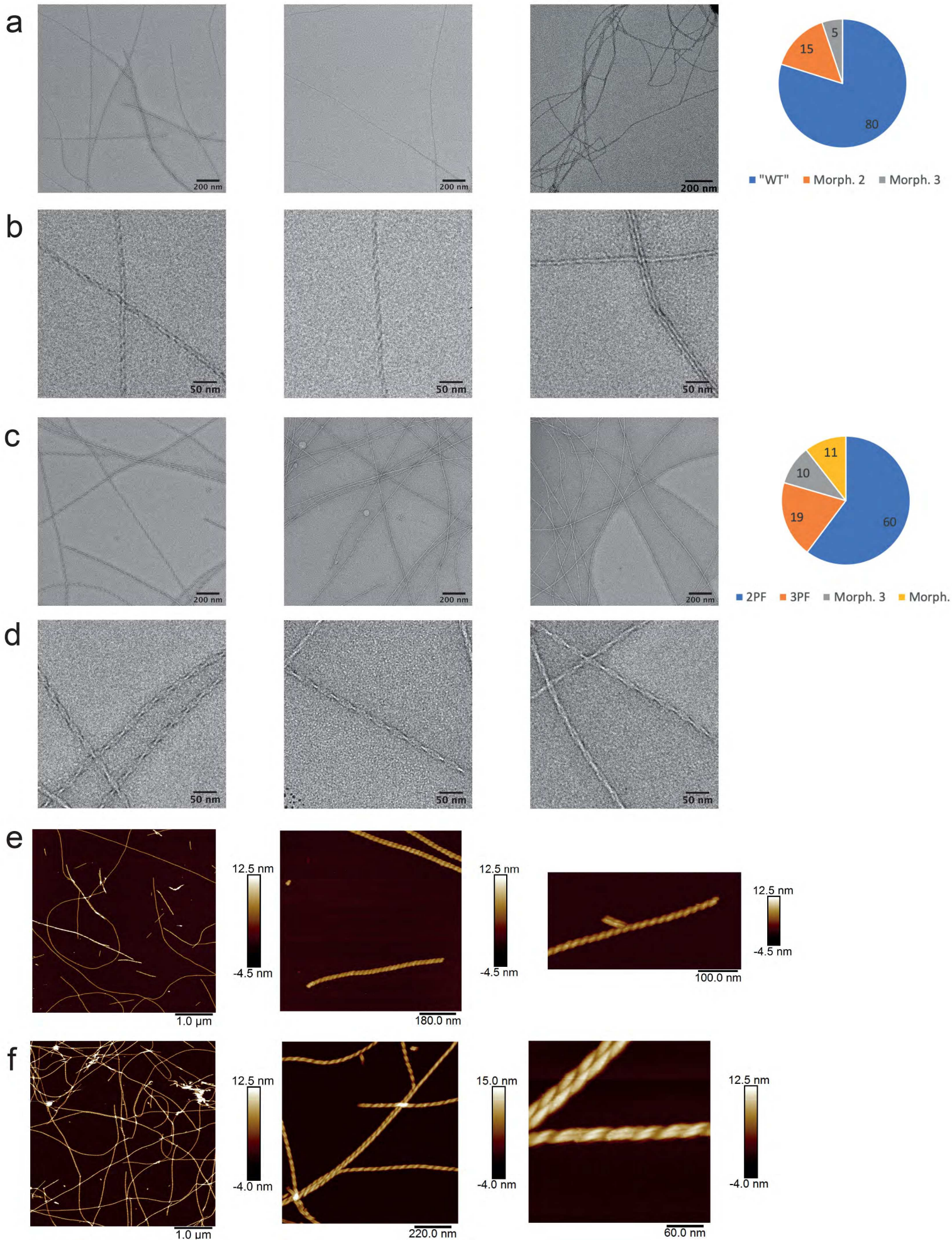
a
200 nm
200 nm
200 nm
5
15
80
"WT"
Morph. 2
Morph. 3
b
50 nm
50 nm
50 nm
c
200 nm
200 nm
200 nm
11
10
19
60
2PF
3PF
Morph. 3
Morph. 4
d
50 nm
50 nm
50 nm
e
12.5 nm
-4.5 nm
1.0 µm
12.5 nm
-4.5 nm
180.0 nm
12.5 nm
-4.5 nm
100.0 nm
f
12.5 nm
-4.0 nm
1.0 µm
15.0 nm
-4.0 nm
220.0 nm
12.5 nm
-4.0 nm
60.0 nm

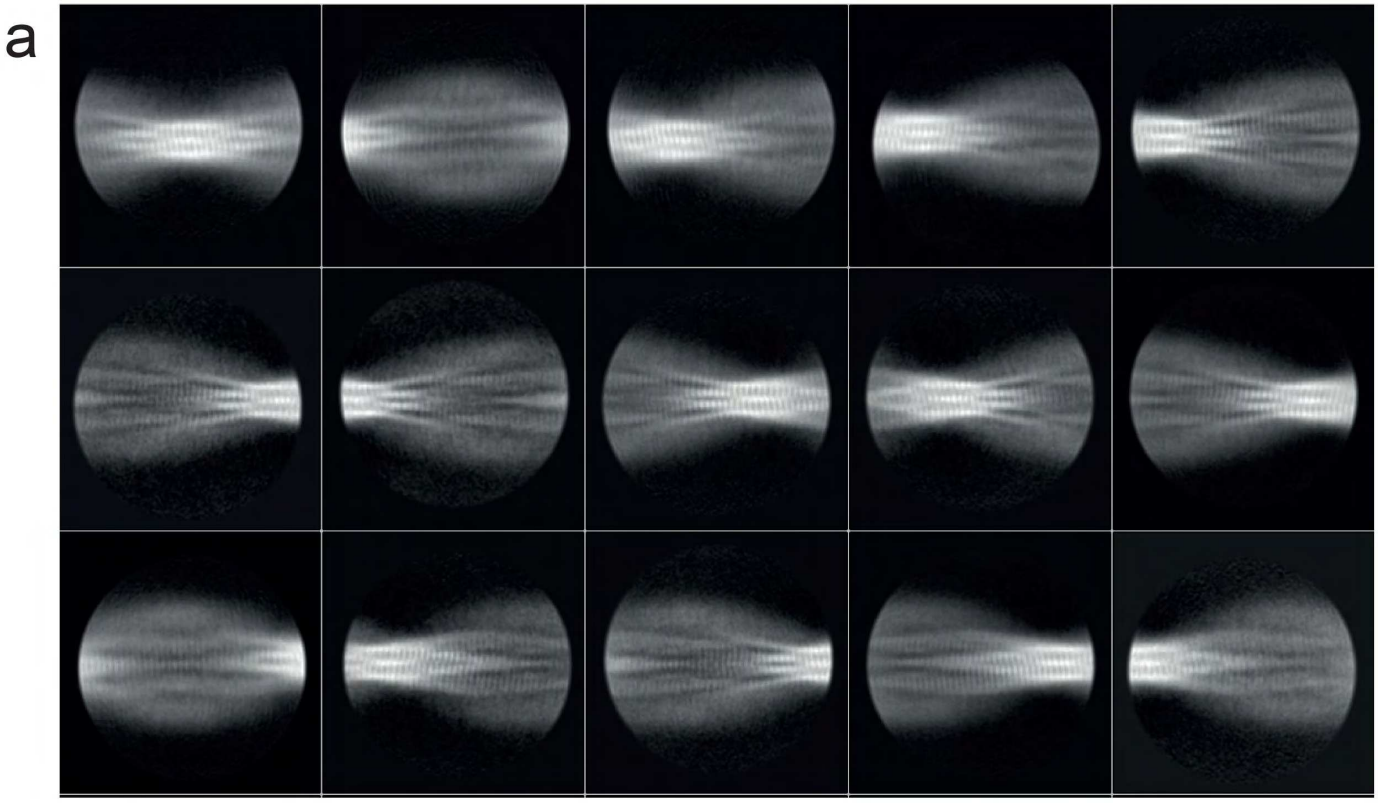
a

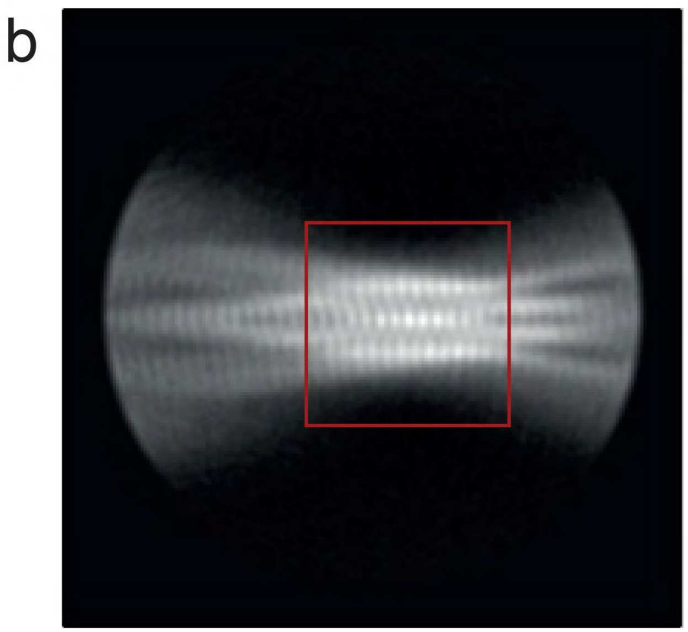
b

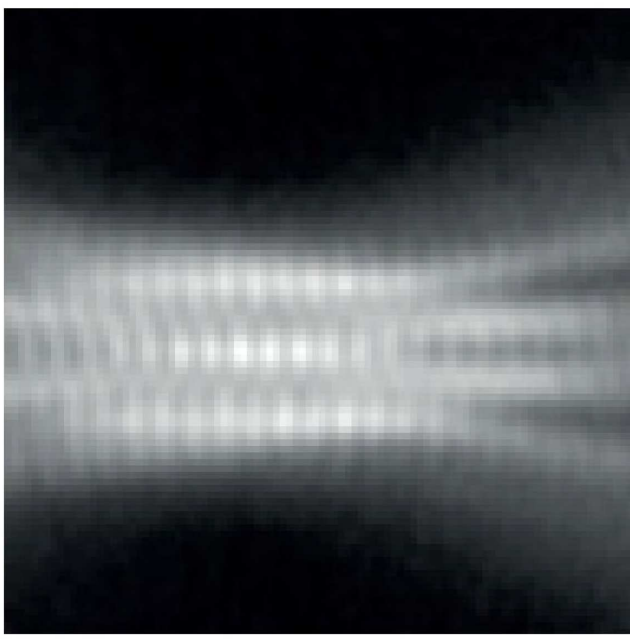
c

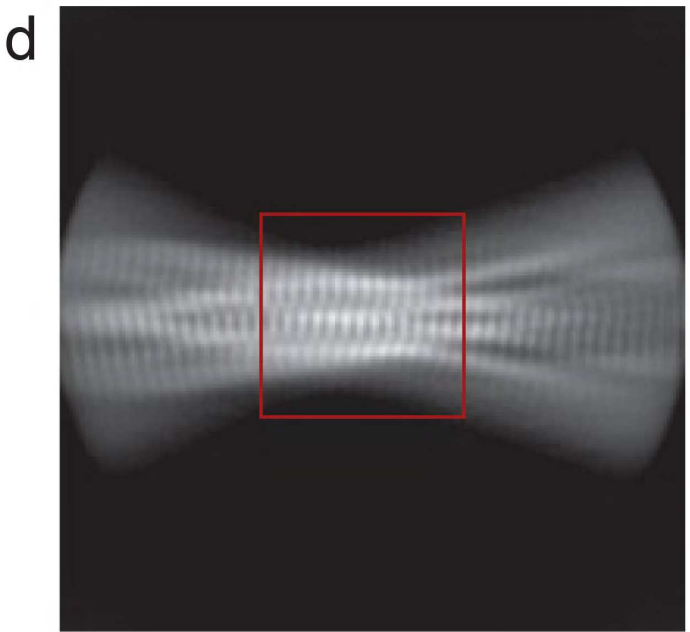
d

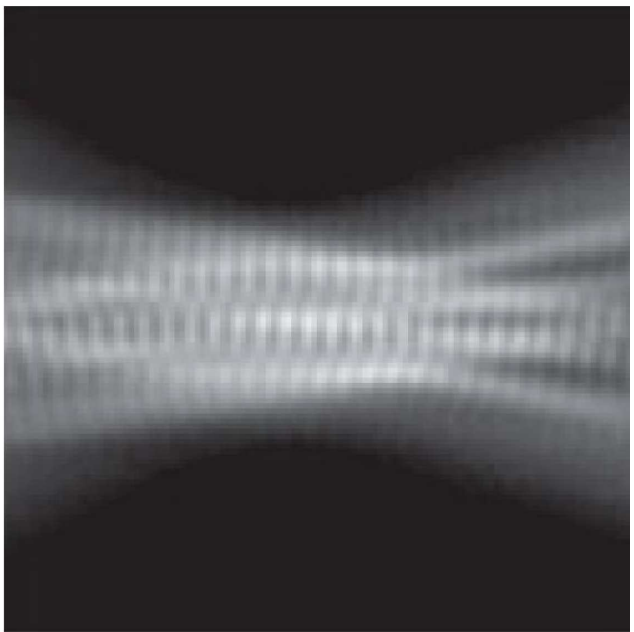
e

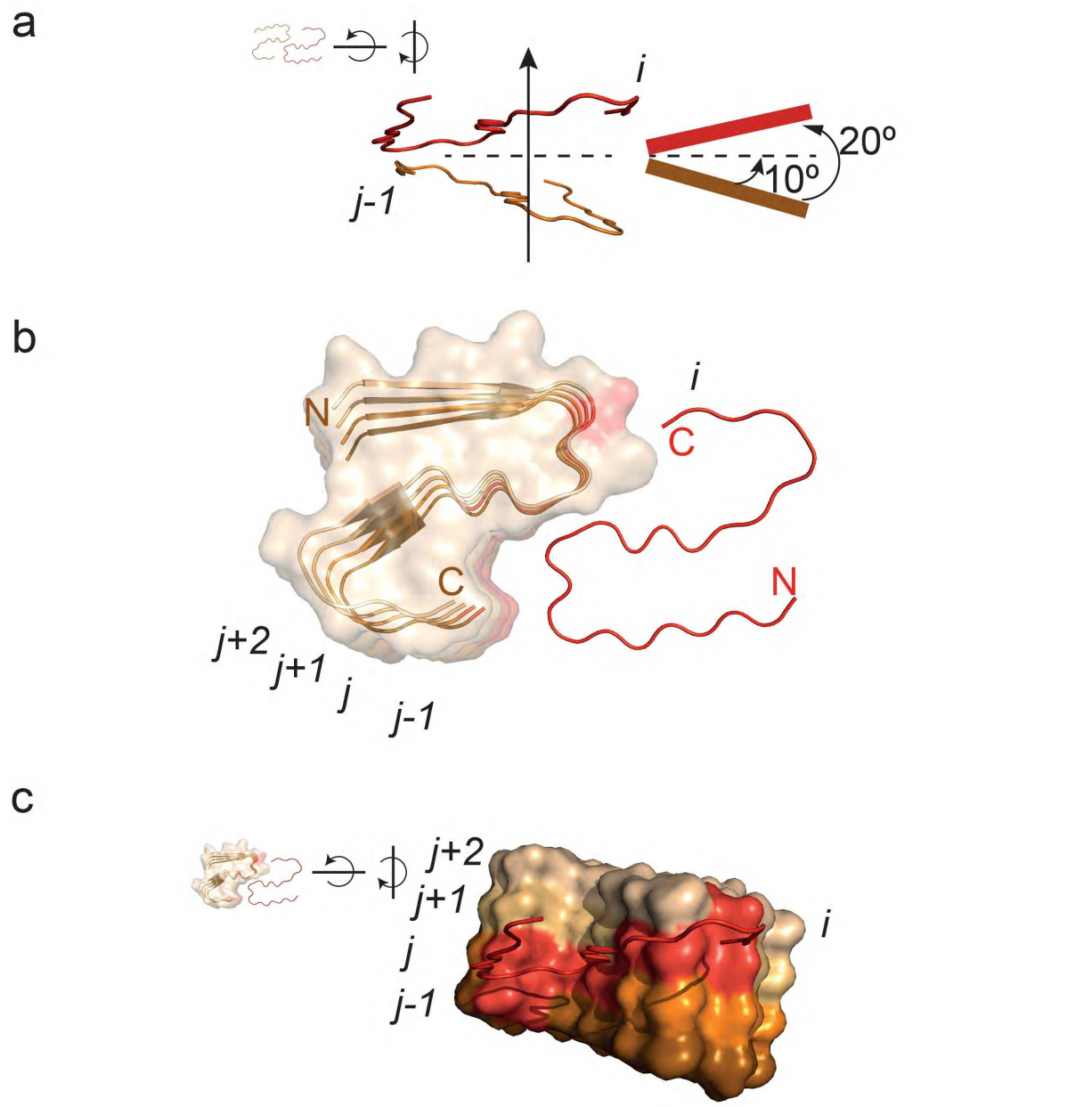
a
i
j-1
20°
10°
b
N
C
i
C
N
j+2
j+1
j
j-1
c
j+2
j+1
j
j-1
i

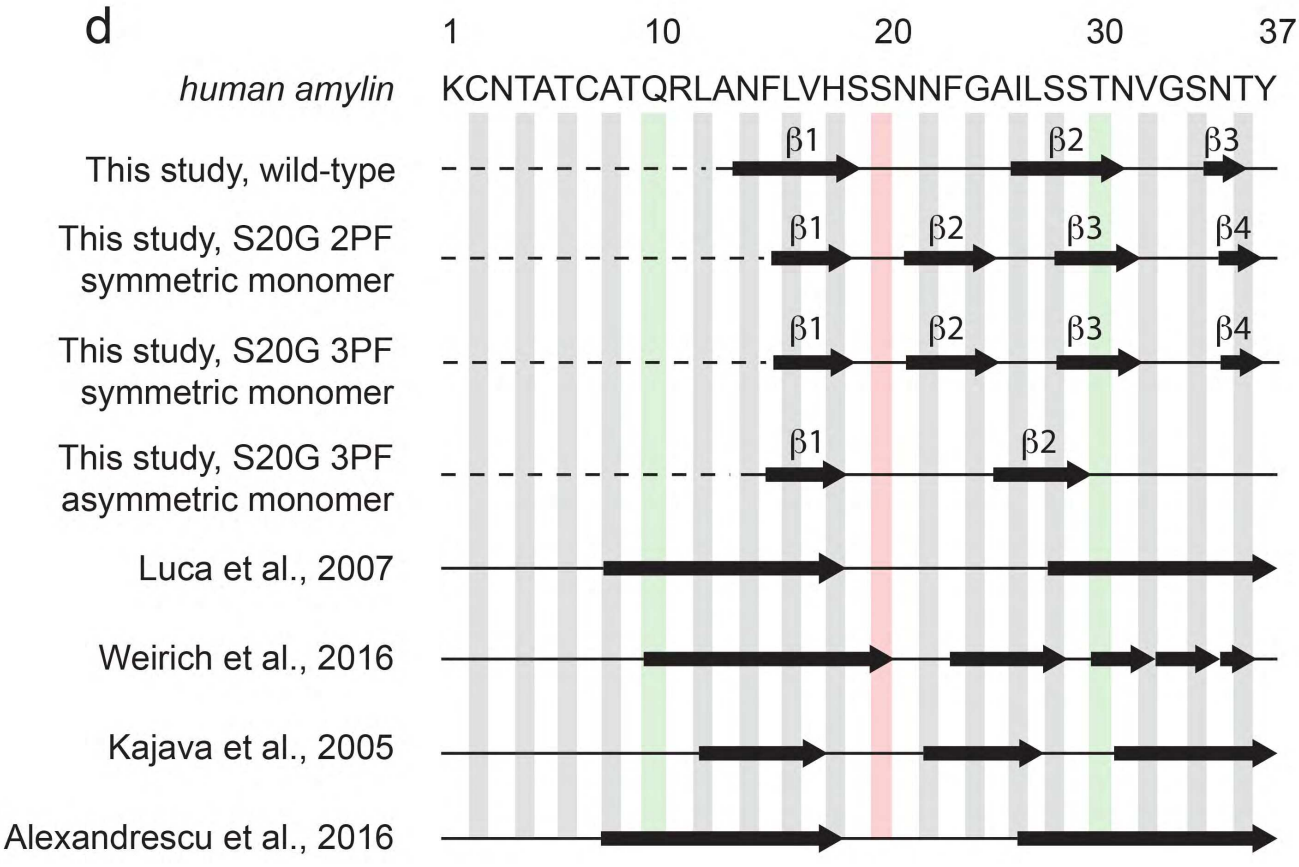
d
1
10
20
30
37
human amylin
KCNTATCATQRLANFLVHSSNNFGAILSSTNVGSNTY
This study, wild-type
β1
β2
β3
This study, S20G 2PF symmetric monomer
β1
β2
β3
β4
This study, S20G 3PF symmetric monomer
β1
β2
β3
β4
This study, S20G 3PF asymmetric monomer
β1
β2
Luca et al., 2007
Weirich et al., 2016
Kajava et al., 2005
Alexandrescu et al., 2016

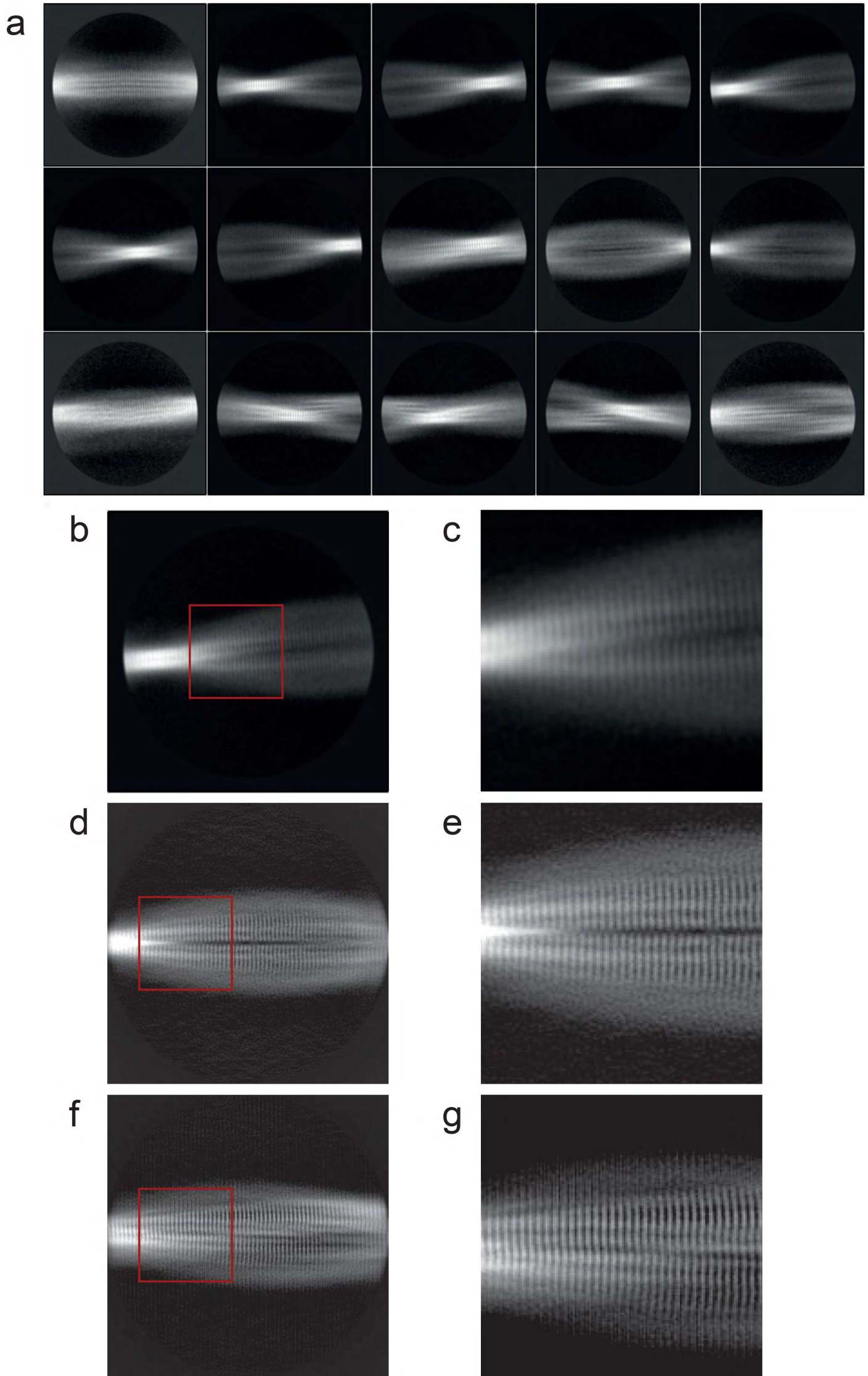
a
b
c
d
e
f
g

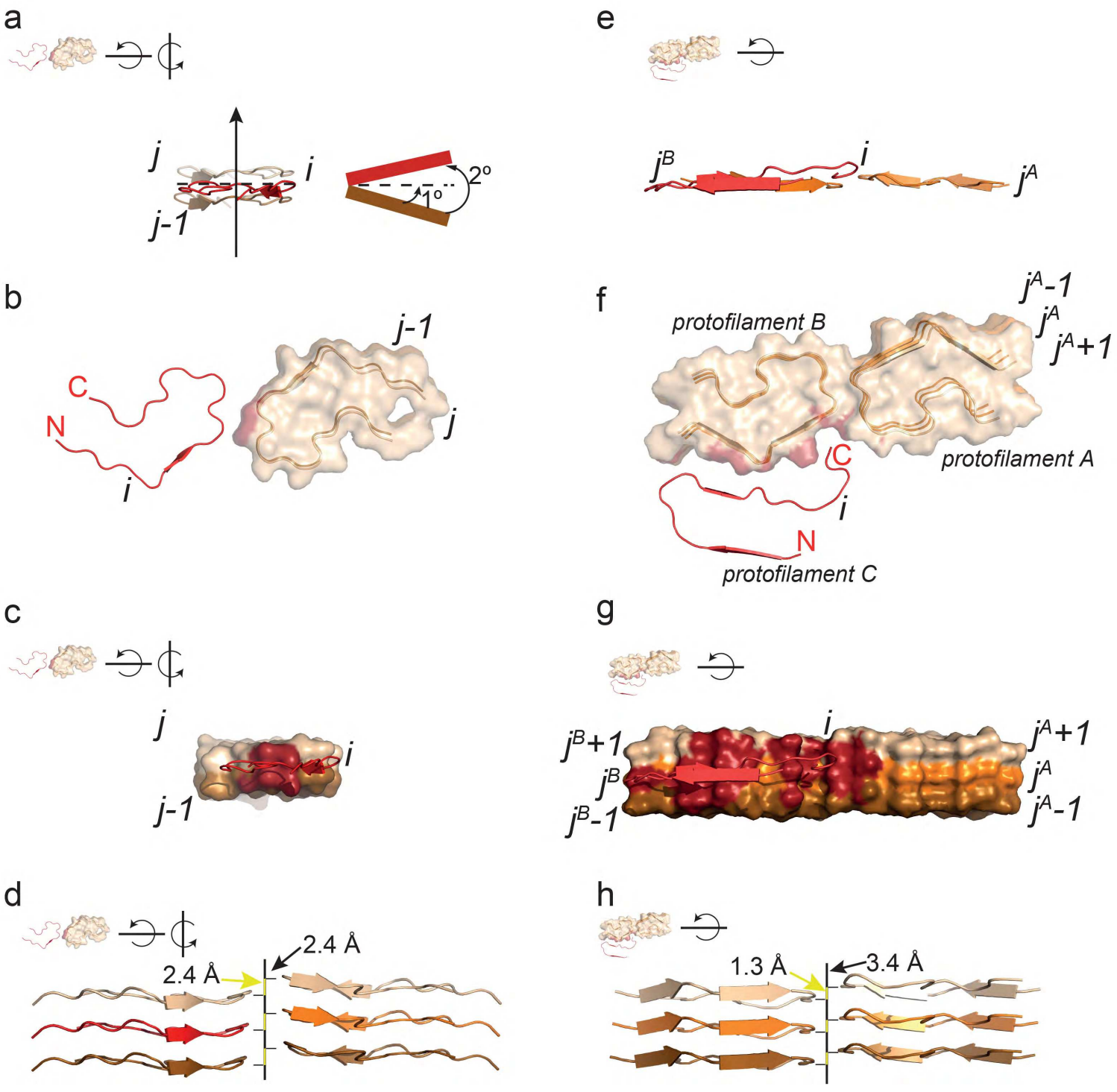
a
j
i
j-1
2°
1°
b
j-1
C
N
i
j
c
j
i
j-1
d
2.4 Å
2.4 Å
e
j^B
i
j^A
f
j^A-1
j^A
j^A+1
protofilament B
protofilament A
C
i
N
protofilament C
g
j^B+1
i
j^A+1
j^B
j^A
j^B-1
j^A-1
h
1.3 Å
3.4 Å

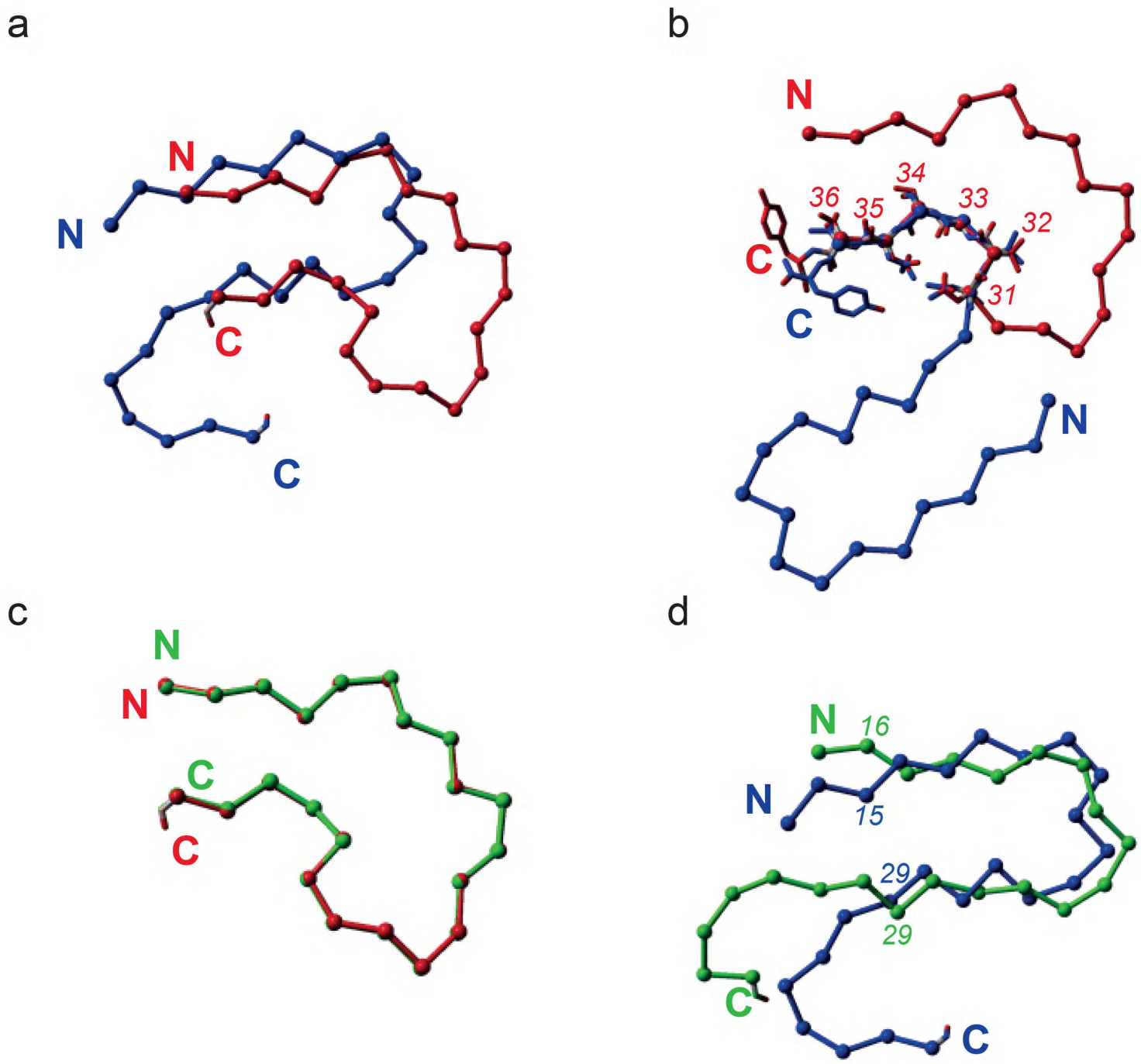
a
N
N
C
C
b
N
34
36
35
33
32
C
31
C
N
c
N
N
C
C
d
N
16
N
15
29
29
C
C

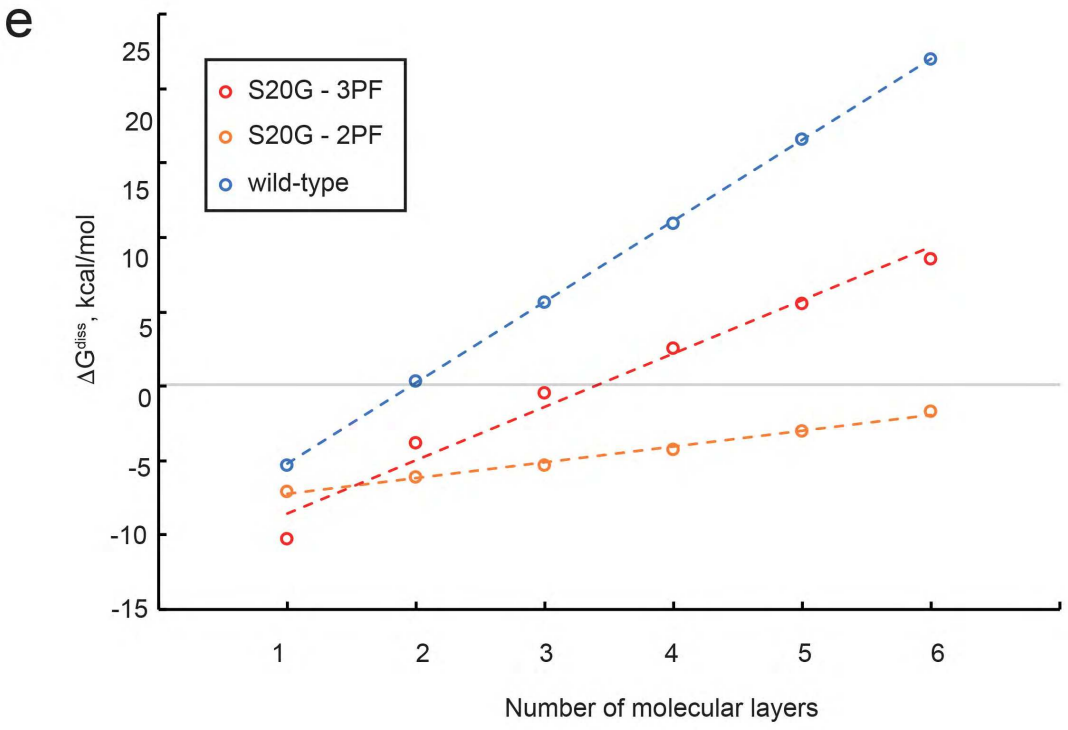
e
S20G - 3PF
S20G - 2PF
wild-type
ΔG^diss, kcal/mol
25
20
15
10
5
0
-5
-10
-15
1
2
3
4
5
6
Number of molecular layers

a

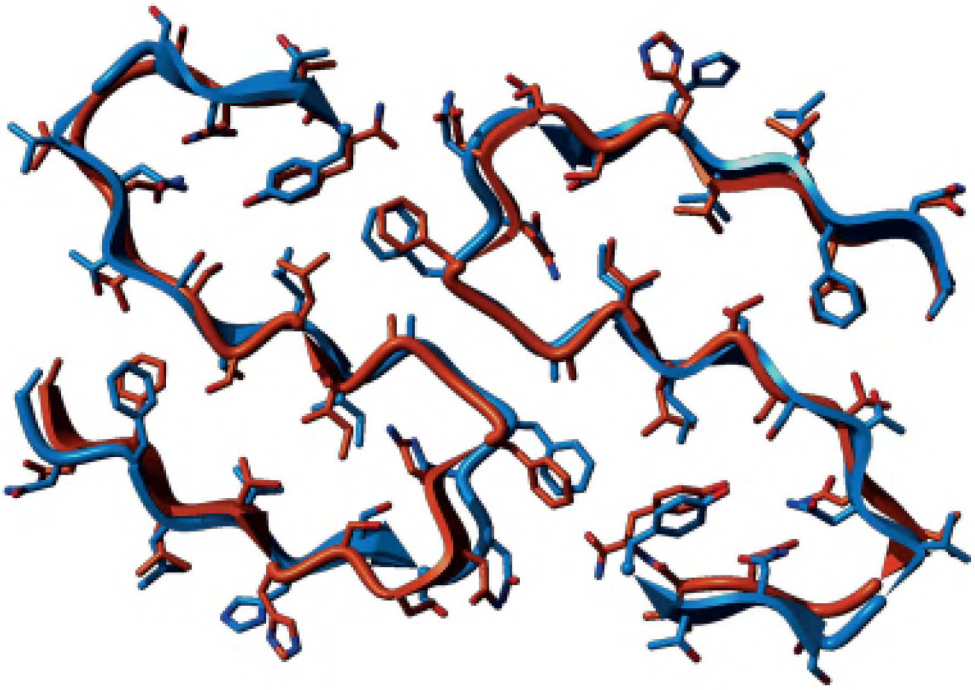

b

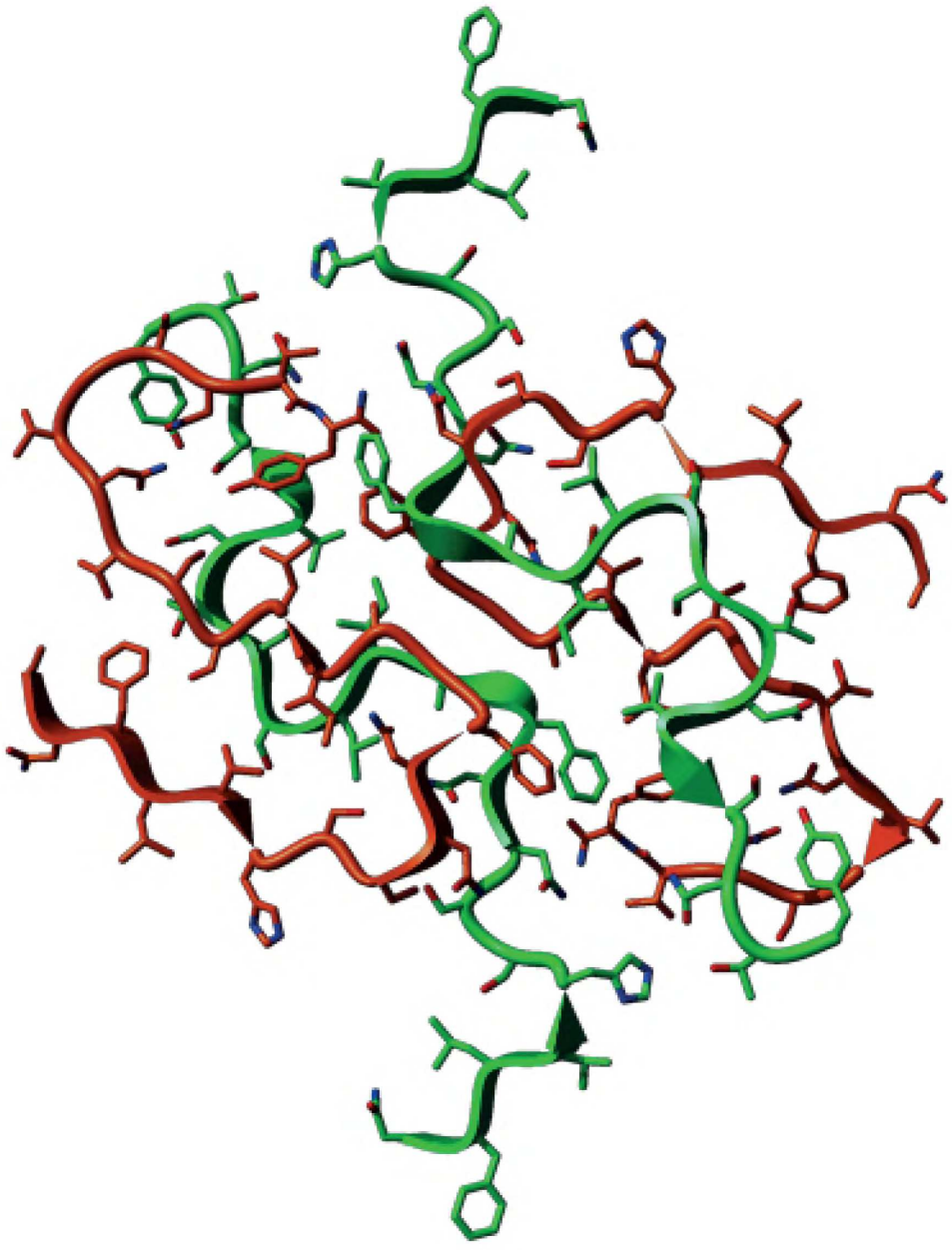

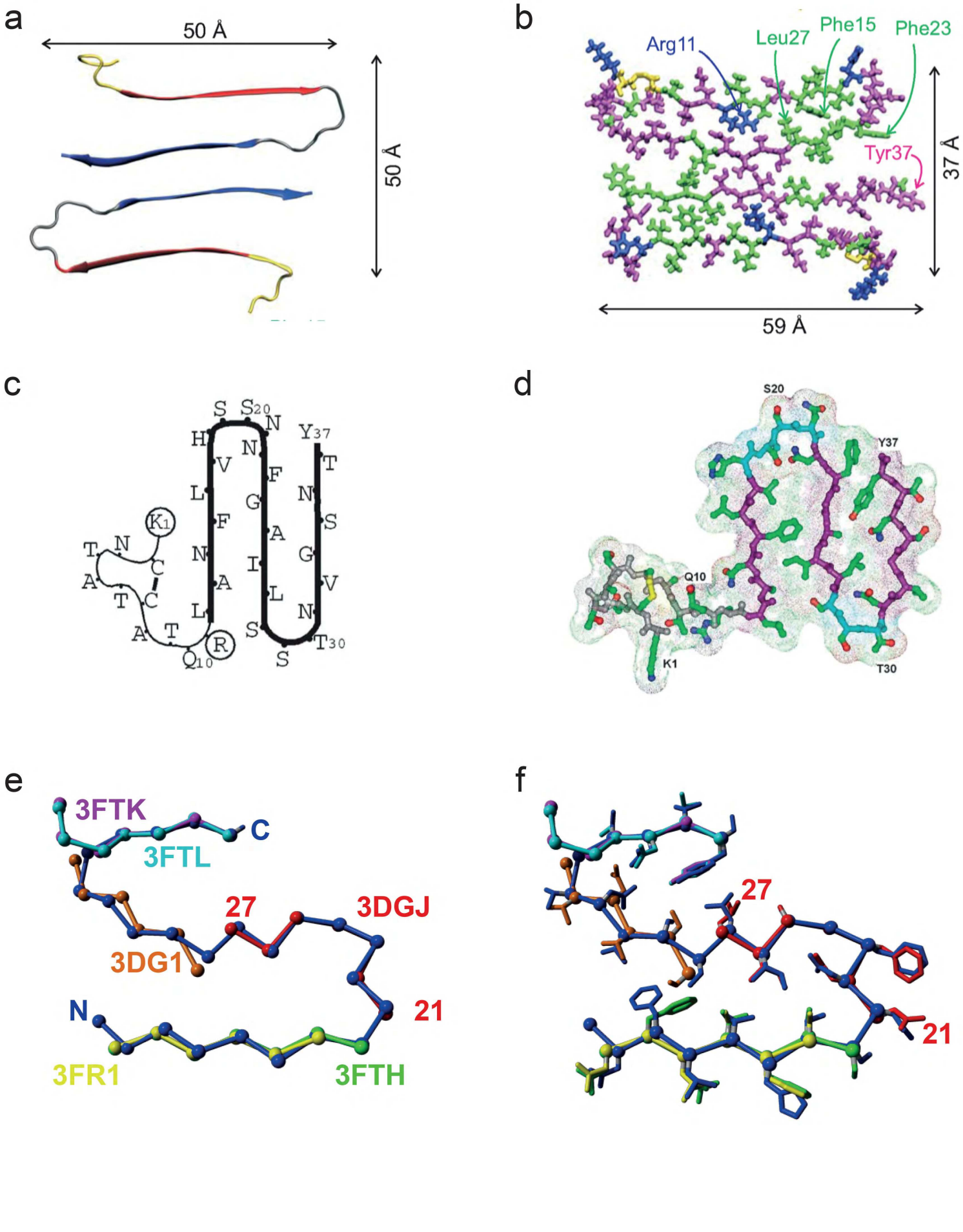
a
50 Å
50 Å
b
Arg11
Leu27
Phe15
Phe23
Tyr37
37 Å
59 Å
c
S S20 N
H N Y37
V F T
L G N
F A S
K1 N G
T N I V
C A
A T C L
T N
A T L
R S N
Q10 S T30
d
S20
Y37
Q10
K1
T30
e
3FTK
C
3FTL
27
3DGJ
3DG1
N
21
3FR1
3FTH
f
27
21

a

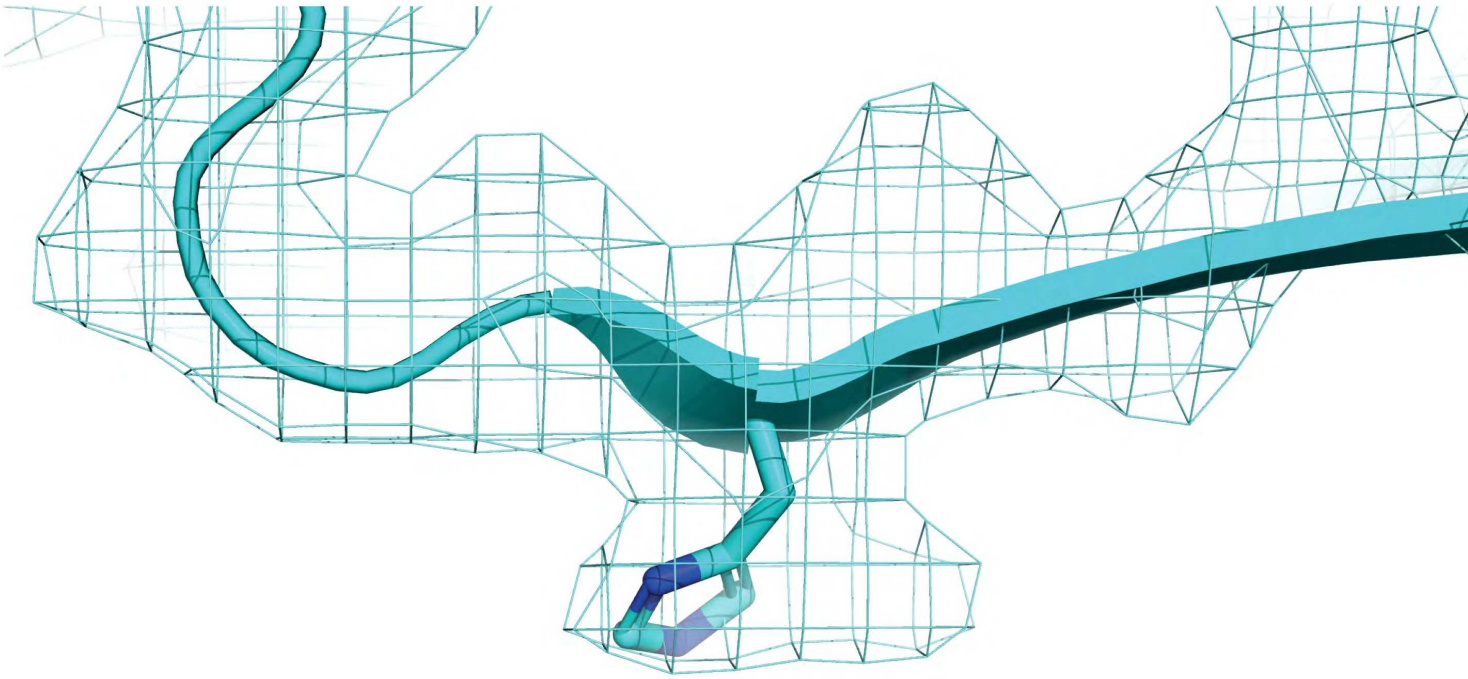

b

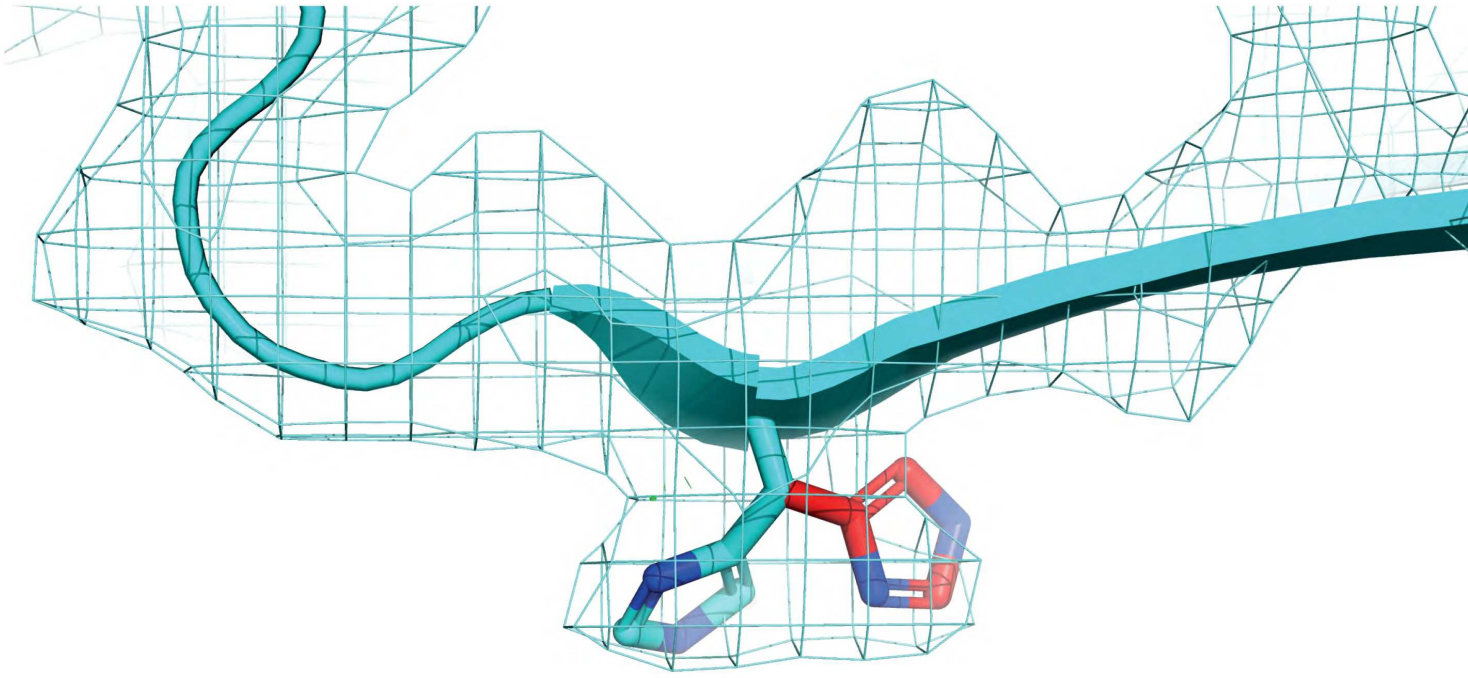

a

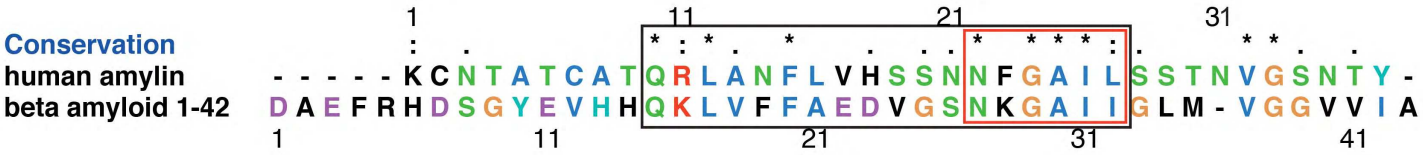
1
11
21
31
Conservation
human amylin - - - - - K C N T A T C A T Q R L A N F L V H S S N N F G A I L S S T N V G S N T Y -
beta amyloid 1-42 D A E F R H D S G Y E V H H Q K L V F F A E D V G S N K G A I I G L M - V G G V V I A
1
11
21
31
41

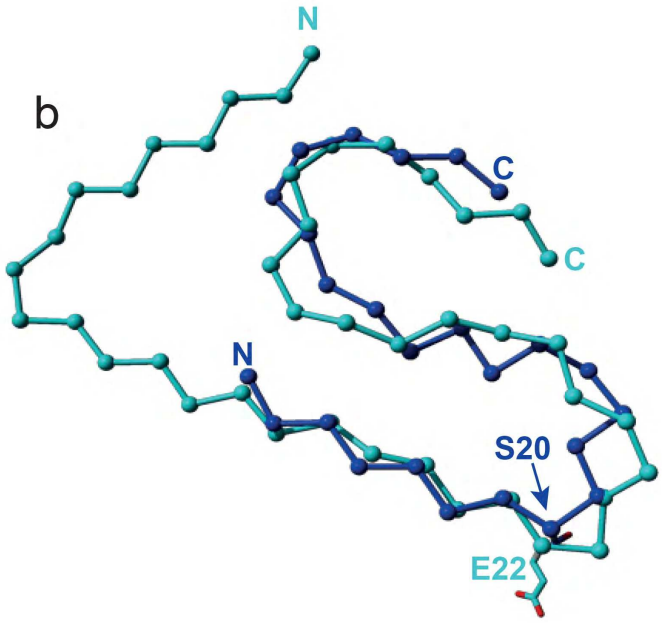
b
N
C
C
N
S20
E22

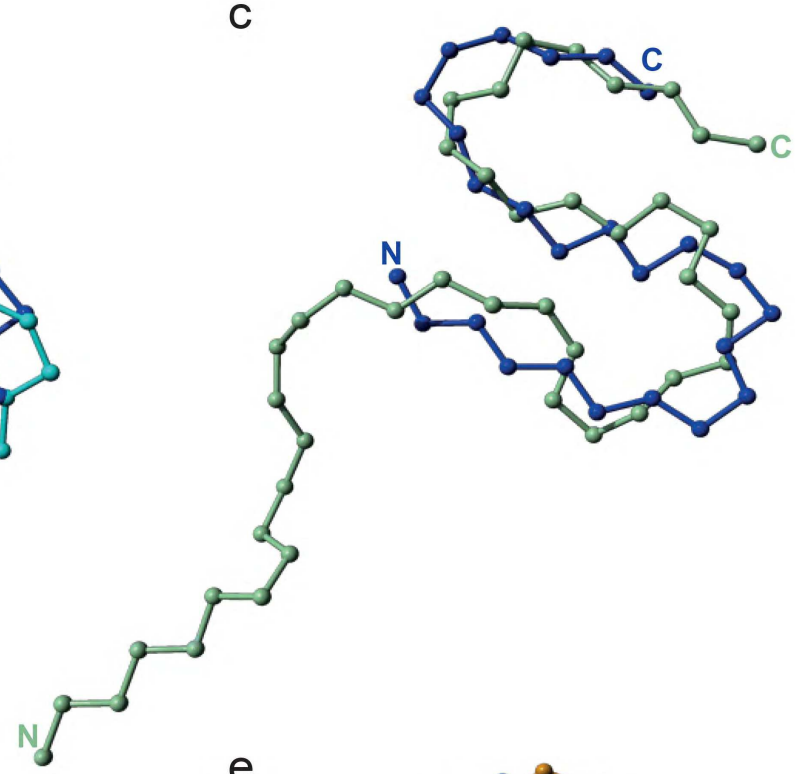
c
C
C
N
N

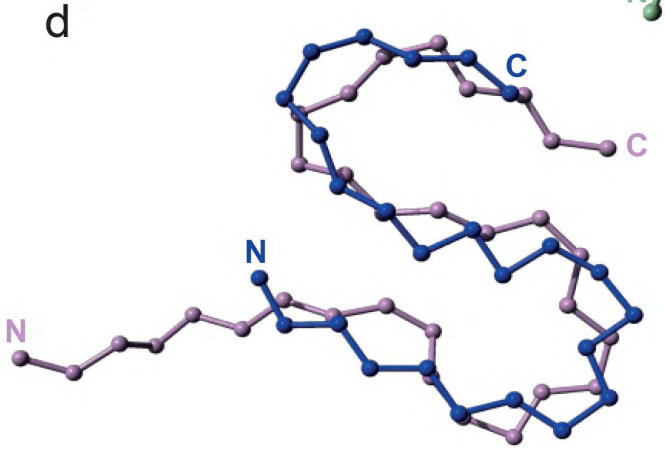
d
C
C
N
N

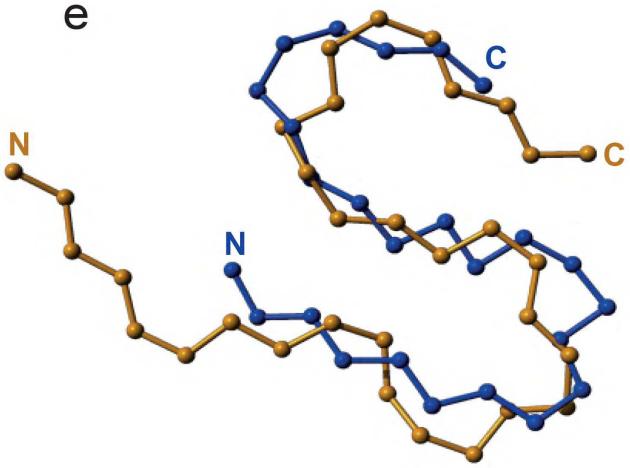
e
C
C
N
N